

ANALYZING THE TRAINING DYNAMICS OF IMAGE RESTORATION TRANSFORMERS: A REVISIT TO LAYER NORMALIZATION

006 **Anonymous authors**

007 Paper under double-blind review

ABSTRACT

013 This work analyzes the training dynamics of Image Restoration (IR) Transform-
 014 ers and uncovers a critical yet overlooked issue: conventional LayerNorm (LN)
 015 drives feature magnitudes to diverge to a *million scale* and collapses channel-wise
 016 entropy. We analyze this in the perspective of networks attempting to bypass Lay-
 017 erNorm’s constraints, which conflict with IR tasks. Accordingly, we address two
 018 misalignments: 1) *per-token normalization* that disrupts spatial correlations, and
 019 2) *input-independent scaling* that discards input-specific statistics. To address this,
 020 we propose Image Restoration Transformer Tailored Layer Normalization (*i*-LN),
 021 a simple drop-in replacement that normalizes features holistically and adaptively
 022 rescales them per input. We provide theoretical insights and empirical evidence that
 023 this design effectively captures important spatial correlations and better preserves
 024 input-specific statistics throughout the network. Experimental results verify that
 025 the proposed *i*-LN consistently outperforms vanilla LN on various IR tasks.

1 INTRODUCTION

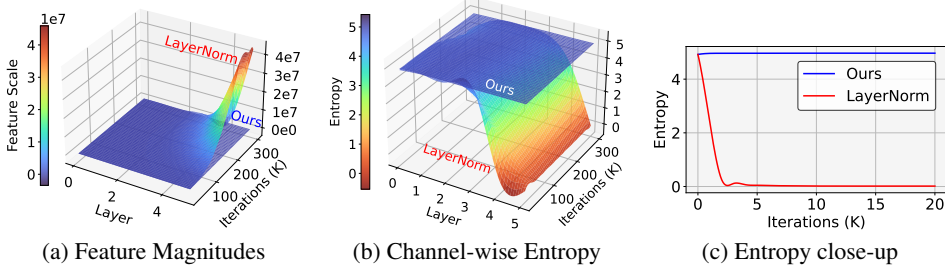
029 Image restoration (IR) aims to reconstruct high-quality images from degraded inputs. With the success
 030 of Vision Transformers (Dosovitskiy et al., 2020), Transformer-based architectures have been actively
 031 adopted for IR tasks and are now a common standard for high-performance IR backbone (Liang
 032 et al., 2021; Chen et al., 2023a; Hsu et al., 2024). However, despite recent architectural advances, the
 033 underlying training dynamics of IR Transformers remain underexplored.

034 This inspires us to take a closer look at their internal behavior, leading us to uncover a critical yet
 035 overlooked phenomenon: feature magnitudes diverge dramatically, reaching scales up to a *million*,
 036 while channel-wise feature entropy drops sharply (Fig.1). Interestingly, this phenomenon aligns with
 037 previous studies (Karras et al., 2020; Wang et al., 2022a), which similarly observed visual artifacts
 038 and abnormal features when coupled with specific normalization layers. However, discussions specific
 039 to the unique requirements of IR tasks and IR Transformers were not made.

040 Building on these insights, we hypothesize that the observed feature divergence in IR Transformers
 041 arises from networks attempting to circumvent LayerNorm (LN), due to constraints of LN that do
 042 not align with the unique requirements of IR tasks. Accordingly, we identify two key mismatches
 043 between LayerNorm and IR tasks; supported by both theoretical insights and extensive empirical
 044 analysis. First, LayerNorm operates in a per-token manner, without considering inter-pixel (token)
 045 relationships. This disrupts the spatial correlations in input features, an aspect crucial for high-fidelity
 046 image restoration. Second, it maps intermediate features into a unified normalized space, limiting the
 047 range flexibility of internal representations. This thereby disregards the input-dependent statistical
 048 variability (Lim et al., 2017b) that is inherent in IR tasks. Together, these mismatches significantly
 049 hinder IR Transformer’s ability to accurately preserve low-level features throughout the network,
 050 which is necessary for faithful image restoration. While one intuitive solution could be the complete
 051 removal of normalization layers as prior works have done (Lim et al., 2017b; Wang et al., 2018;
 052 Karras et al., 2020; 2024), our experimental observations highlight significant training instability
 053 when normalization is entirely omitted from IR Transformers (Tab.1); the network fails to converge.

In this work, we show that these issues can be addressed in a surprisingly simple manner; leading to
 significant stability and substantial performance gain. We propose the *Image Restoration Transformer*

054
055
056
057
058
059
060
061
062
063



064
065
066
067
068
069
070
071
Figure 1: **Visualization of feature magnitudes and channel-wise entropy during training of an Image Restoration (IR) Transformer using conventional LayerNorm (LN) and *i*-LN (Ours).**
(a) Evolution of feature magnitudes across layers and training iterations, highlighting the dramatic divergence (to million-scale) under conventional LN. **(b-c)** Channel-wise entropy with LN drops sharply at the very early stage of training, indicating the emergence of acute peaks hidden in specific channels. Ours *i*-LN exhibits well-distributed activation across channels and significant stability.

072
073
074
075
076
077
078
079
080
081
082
083
Tailored Layer Normalization (i-LN), which acts as a drop-in replacement to conventional (vanilla) LayerNorm by better aligning with the unique requirements of IR tasks. Instead of normalizing each token independently, we propose to apply normalization across the entire spatio-channel dimension within IR Transformers (Fig.3), effectively preserving spatial correlations among tokens, contrary to vanilla per-token LayerNorm. Furthermore, We rescale features with the normalization parameters after each attention and feed-forward layer, explicitly enabling range flexibility and accounting for input-dependent variations in internal feature statistics. Together, these modifications effectively preserve low-level feature statistics throughout the network, better aligning with the requirements of IR tasks. Extensive experiments show that *i*-LN leads to both stable training dynamics with improved performance across various IR benchmarks. Additionally, we observe cues suggesting robustness under reduced-precision configurations and improved spatial correlation modeling.

2 METHOD

2.1 REVISITING LAYER NORMALIZATION

088
089
090
091
Observation (Abnormal Feature Statistics). Our initial analysis focuses on tracking the trajectory of internal features during the training of IR Transformers. We visualize the squared mean of intermediate features at each basic building block of the network, following (Karras et al., 2024). We select the x4 SR task using the HAT (Chen et al., 2023a) model as the representative IR task (Fig.1).

092
093
094
095
096
097
098
099
100
The analysis reveals that feature statistics diverge dramatically, reaching values up to a *million* scale. To pinpoint the origins of this feature divergence, we analyze the feature entropy across the channel-axis. Analysis demonstrates a sharp decrease in feature entropy, which indicates the presence of channels with extreme values that dominate the statistics. Since these extreme values are unusual, this motivates us to further investigate. Accordingly, we analyze the training dynamics across configurations by varying the network scale (Fig.2a2b), varying the IR tasks (Fig.2c), and varying the normalization scheme (Fig.4); and observe that this phenomenon occurs across all configurations utilizing standard IR Transformers. While this type of hidden abnormal behavior aligns with the observations in prior studies (Karras et al., 2020; Wang et al., 2018; 2022a), further discussion did not gain much attention, especially regarding the unique properties and requirements of IR Transformers.

101
102
103
104
105
In the following, we provide further insights into this phenomenon by examining the characteristics of LayerNorm (LN), the de facto normalization in IR Transformers. We start by defining the spatial relationship between pixels (i.e., inter-pixel structure), and further show that conventional LayerNorm cannot preserve this. For simplicity, we neglect the affine parameters for theoretical analysis.

106
107
Definition 1 (Inter-pixel Structure and Preservation). *Let $x \in \mathbb{R}^{L \times C}$ be a feature map with L tokens. We write the ℓ -th token as $x_\ell \in \mathbb{R}^C$ and the c -th element of it as $x_{\ell,c} \in \mathbb{R}$. The inter-pixel structure of a feature map is given by the set of relative differences $\Delta x := \{x_\ell - x_k : 1 \leq \ell, k \leq L\}$.*

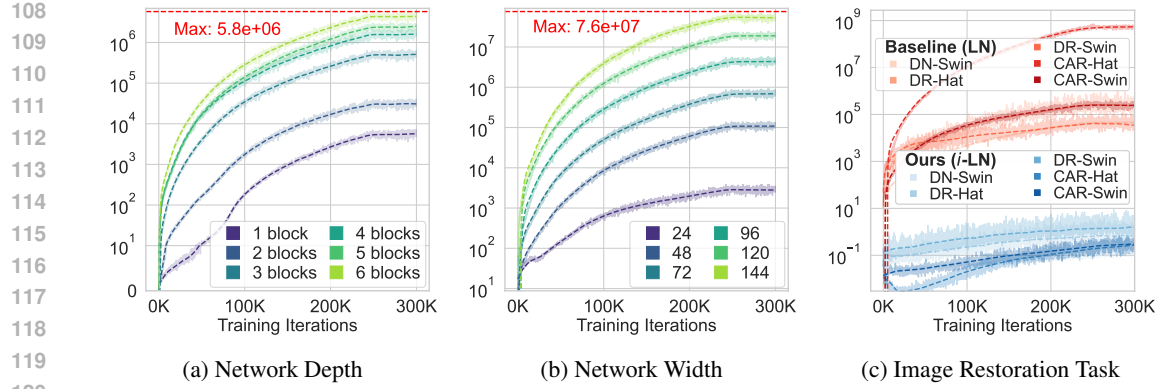


Figure 2: **Feature magnitude evolution in IR Transformers across different settings.** (a-b) Feature divergence signifies as the network scales. (c) Feature divergence appears across various Transformer backbones and IR tasks: super-resolution (SR), denoising (DN), deraining (DR), JPEG compression artifact removal (CAR), demonstrating that this phenomenon is widespread. It can be effectively mitigated by simply replacing conventional LayerNorm with the proposed *i*-LN.

Definition 2 (Structure Preserving Transformation). *A transformation T is said to preserve inter-pixel structure up to scale if there exists a homothety $H(x) = ax + b$, with $a > 0$ and $b \in \mathbb{R}^C$, such that*

$$T(x_\ell) - T(x_k) = H(x_\ell - x_k) = a(x_\ell - x_k) \quad \text{for all } \ell, k.$$

Such maps preserve all angles and pairwise distance ratios, and correspond to a single global shift and uniform scaling across all tokens. For $a = 1$, T is said to preserve structure absolutely.

Intuitively, consider x as a point cloud in \mathbb{R}^C , where each point represents a token. A structure-preserving transformation may only uniformly scale and shift the entire cloud. That is, the overall shape of the point cloud should be preserved up to a single global scaling factor and translation.

Vanilla Per-token LayerNorm (Baseline). Conventional Transformer architectures utilize the per-token LayerNorm (LN) as the de facto normalization scheme which operates as follows:

$$\text{LN}(x_\ell) = \gamma \frac{1}{\sqrt{\sigma_\ell^2 + \epsilon}} (x_\ell - \mu_\ell) + \beta, \quad \mu_\ell = \mathbb{E}_c[x_{\ell,c}], \quad \sigma_\ell^2 = \mathbb{E}_c[(x_{\ell,c} - \mu_\ell)^2], \quad (1)$$

where $\mathbb{E}_c[\cdot]$ is taken over the channel dimension c , and $\gamma, \beta \in \mathbb{R}^c$ are each affine parameters applied after the normalization step, and LN operates for each token x_ℓ given the entire input feature x .

Proposition 1. (Vanilla LayerNorm fails to preserve structure). *Let T_{LN} be the normalization in vanilla per-token LN. Then, in general, there do not exist $a > 0$ and an orthogonal Q such that*

$$T_{\text{LN}}(x_\ell) - T_{\text{LN}}(x_k) = a Q (x_\ell - x_k) \quad \text{for all } x_\ell, x_k,$$

Thus T_{LN} is not even conformal on the token set. Since homotheties are strict subclasses of conformal maps, T_{LN} is not a homothety and therefore it does not preserve inter-pixel structure in general.

Remark. The exception arises in degenerate cases where all tokens share identical per-token mean and variance, in which case a similarity map can exist (i.e., inter-pixel structure is preserved). Such cases are extremely rare in practice. Our intuition is that since LN cannot naturally preserve inter-pixel structure, networks learn to generate large magnitude features regardless of the input, thereby, manipulate the overall feature statistic to behave similarly to this exceptional degenerate scenario.

Inspired by prior observations, we hypothesize that feature divergence arises from a fundamental mismatch between the requirements of IR tasks and the constraints imposed by LayerNorm, leading us to propose a tailored normalization scheme that aligns with the unique requirements of IR tasks.

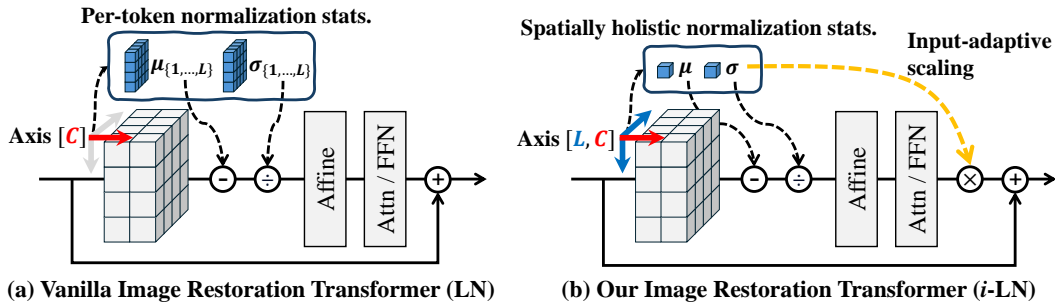


Figure 3: Comparison between IR Transformer blocks using conventional per-token LayerNorm (LN) and our proposed *i-LN*. Contrary to conventional LN, which normalizes each token independently, our *i-LN* applies holistic normalization across the entire spatio-channel dimension, preserving essential spatial correlations between tokens. Additionally, *i-LN* input-adaptively rescales features after the attention (Attn) and feedforward (FFN) layers, thereby better preserving input statistics and allowing feature range flexibility. These together enable IR Transformers to preserve low-level characteristics of input throughout the network, aligning with the unique requirements of IR.

2.2 TAILORING LAYERNORM FOR IMAGE RESTORATION TRANSFORMERS

Spatially Holistic Normalization (LN*). We propose a simple variant of LN that improves in preserving inter-token spatial relationships of input features, which we refer to as LN*. Instead of normalizing each token individually as LN, we derive normalization statistics from the entire spatio-channel dimension of the input feature as follows:

$$\text{LN}^*(x) = \gamma \frac{1}{\sqrt{\sigma^2 + \epsilon}} (x - \mu) + \beta, \quad \mu = \mathbb{E}_{\ell,c}[x_{\ell,c}], \quad \sigma^2 = \mathbb{E}_{\ell,c}[(x_{\ell,c} - \mu)^2], \quad (2)$$

where the expectation $\mathbb{E}_{\ell,c}[\cdot]$ is taken over both spatial (ℓ) and channel dimensions (c). This straightforward modification effectively mitigates the issue raised by the per-token operation in vanilla per-token LayerNorm. While normalization methods in CNNs already inherently work in a spatially holistic manner, the implications of such holism in normalization and the corresponding spatial structure corruption without it have received little attention, particularly in the context of IR Transformers. With this point, the following section aims to provide further intuition and establish connections between holism and spatial structure (i.e., inter-pixel structure) preservation.

Proposition 2. (LN* preserves structure). Let T_{LN^*} be the normalization defined by LN*, with global mean μ and std. $\sigma > 0$ computed over all tokens and channels. Then for any two tokens x_ℓ, x_k ,

$$T_{\text{LN}^*}(x_\ell) - T_{\text{LN}^*}(x_k) = (1/\sigma)(x_\ell - x_k).$$

Thus, T_{LN^*} is a homothety, and accordingly, preserves spatial structure up to a global scale.

Remark. In short, LN* is structure-preserving up to one missing scalar (i.e., the global scale). We handle this loss of information by explicitly reintroducing it later, as described below.

Preserving Input Dependent Statistics. We further tailor the normalization operator to better suit the requirements of IR tasks. Specifically, we address the issue of input-blind normalization. While IR tasks require the preservation of input-dependent feature statistics for faithful reconstruction, both conventional LayerNorm and even the holistic LN* overlooks this aspect by mapping features into a unified normalized space. Although normalization improves training stability, it also causes the model to lose critical input-dependent information (i.e., the missing global scale term of inter-pixel structure) by restricting the range flexibility of internal representations (Lim et al., 2017b).

Accordingly, we propose a simple input-adaptive rescaling strategy that effectively tackles this issue. We rescale the output of Attention and FFN by their standard deviation computed in the preceding normalization process as the yellow line in Fig.3b, which we refer to as *i-LN*. Accordingly, a typical Attention or FFN block B could be further improved by coupling with *i-LN* as follows:

$$B(x; f, i\text{-LN}) = x + \sqrt{\sigma^2 + \epsilon} \cdot f(\text{LN}^*(x)), \quad (3)$$

Idx	Method	SH	Set14		BSD100		Urban100		Manga109	
			PSNR	SSIM	PSNR	SSIM	PSNR	SSIM	PSNR	SSIM
1	LayerNorm	✗	28.79	.7876	27.68	.7411	26.55	.8015	31.01	.9150
2	LayerScale	✗	28.89	.7887	27.76	.7426	26.75	.8058	31.37	.9178
3	RMSNorm	✗	28.88	.7879	27.74	.7417	26.67	.8037	31.24	.9165
4	ReZero	✓	28.81	.7861	27.70	.7406	26.41	.7964	31.05	.9147
5	None	✓	-	-	-	-	-	-	-	-
6	InstanceNorm	✓	28.98	.7907	27.80	.7445	27.02	.8136	31.46	.9199
7	BatchNorm [†]	✓	28.95	.7901	27.80	.7442	26.70	.8123	31.39	.9186
8	<i>i</i> -LN (Ours)	✓	29.01	.7915	27.84	.7456	27.17	.8167	31.82	.9228

Table 1: **Comparison between various normalization schemes.** [†] indicates that BatchNorm is evaluated in train-mode. SH indicates the spatial holisticness of the normalization scheme, including the setting without any normalization (None). Experiments are performed for $\times 4$ SR with HAT₁. The best result for each setting is highlighted in **bold**.

where f is either the according Attention or FFN operation of block B . Overall, this reintroduces the original feature statistic lost due to normalization. This simple strategy enables IR Transformers to better preserve the per-instance statistics throughout the network and allows range flexibility to intermediate features. We later show that this leads to an order of magnitude more stable feature distribution (i.e., higher entropy) and overall improved IR performance.

Remark. This simple input-adaptive rescaling strategy explicitly reintroduces the missing global scaling term that LN* could not preserve (which leads to restricted range flexibility).

3 EXPERIMENTS

Training Settings. Since recent works have discrepancies in their detailed training settings (Chen et al., 2024), we reimplement baseline methods and our method under identical settings for fair comparison. Networks for deraining (DR) were trained on Rain13K (Jiang et al., 2020), while DF2K (DIV2K (Agustsson & Timofte, 2017) + Flickr2K (Lim et al., 2017a)) was used for other tasks. Only basic augmentations (random flips, rotations, crops) were applied, without mixing augmentations, progressive patch sizing, or warm-start. In order to provide thorough experimental results under various settings, the overall training budget was reduced as specified in Appendix.5. The representative SwinIR (Liang et al., 2021), HAT (Chen et al., 2023a), and DRCT (Hsu et al., 2024) were used.

Evaluation Settings. Standard benchmarks are employed including: Set5 (Bevilacqua et al., 2012), Set14 (Zeyde et al., 2010), BSD100 (Martin et al., 2001), Urban100 (Huang et al., 2015), Manga109 (Matsui et al., 2017) for SR; CBS68 (Martin et al., 2001), Kodak (Franzen, 1999), McMaster (Zhang et al., 2011), Urban100 for DN; LIVE1 (Sheikh, 2005), Classic5 (Foi et al., 2007), Urban100 (Huang et al., 2015) for CAR; Test100 (Zhang et al., 2019) and Rain100L (Yang et al., 2017) for DR. We crop Urban100 into non-overlapping 256×256 patches due to memory limits for CAR and DN. We report PSNR and SSIM indices. Experiments were performed on NVIDIA A6000s.

3.1 NORMALIZATION SCHEME VARIATION

We analyze the effects of various normalization techniques, including representative normalization schemes as vanilla LayerNorm (LN) (Ba et al., 2016), per-token RMSNorm (RMS) (Zhang & Sennrich, 2019), InstanceNorm (IN) (Ulyanov et al., 2016), BatchNorm (BN) (Ioffe & Szegedy, 2015), and our proposed *i*-LN. Considering previous studies where completely removing normalization from SR networks (Lim et al., 2017b; Wang et al., 2018) led to performance improvements, we additionally tested a similar configuration indicated as *None*, where normalizations are entirely removed.

Further, we investigate the empirical impacts of recent methods designed to stabilize Transformer training: ReZero (RZ) (Bachlechner et al., 2021) and LayerScale (LS) (Touvron et al., 2021). ReZero removes LayerNorm from Transformer blocks and multiplies a learnable zero-initialized scalar to the residual path. Similarly, LayerScale multiplies a near-zero-initialized learnable diagonal matrix to the residual path but reintroduces LayerNorm. Since both methods initially multiply a (near) zero-scale factor to the network output, we consider them as potential solutions to resolve the feature increasing issue in IR tasks. Notably, these methods also align with prior stud-

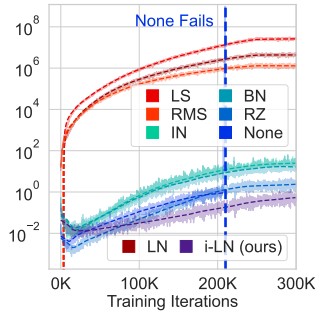


Figure 4: Feature divergence across various normalizations.

270 Table 2: Quantitative comparison between the conventional LayerNorm (LN) and our proposed *i*-LN
 271 across diverse IR tasks. The best result for each setting is highlighted in **bold**.

Backbone	Scale	Set5		Set14		BSD100		Urban100		Manga109		Backbone	Testset	Metric	
		PSNR	SSIM			PSNR	SSIM								
HAT ₁ + LN	$\times 2$	38.14	.9610	33.78	.9196	32.19	.9000	32.16	.9297	38.84	.9778	HAT ₁ + LN	Rain100L	34.35	.9471
HAT ₁ + <i>i</i> -LN	$\times 2$	38.37	.9619	34.08	.9218	32.42	.9028	33.32	.9385	39.69	.9794	HAT ₁ + <i>i</i> -LN	Rain100L	36.20	.9641
DRCT ₁ + LN	$\times 2$	38.19	.9613	33.28	.9197	32.28	.9010	32.60	.9323	39.23	.9785	SwinIR ₁ + LN	Rain100L	33.00	.9434
DRCT ₁ + <i>i</i> -LN	$\times 2$	38.23	.9614	33.86	.9206	32.31	.9014	32.79	.9344	39.40	.9788	SwinIR ₁ + <i>i</i> -LN	Rain100L	34.43	.9527
HAT ₁ + LN	$\times 4$	32.51	.8992	28.79	.7876	27.68	.7411	26.55	.8015	31.01	.9150	HAT ₁ + LN	Test100	29.52	.8905
HAT ₁ + <i>i</i> -LN	$\times 4$	32.72	.9019	29.01	.7915	27.84	.7456	27.17	.8167	31.82	.9228	HAT ₁ + <i>i</i> -LN	Test100	30.14	.9022
DRCT ₁ + LN	$\times 4$	32.50	.8989	28.85	.7871	27.73	.7414	26.63	.8021	31.24	.9169	SwinIR ₁ + LN	Test100	27.45	.8766
DRCT ₁ + <i>i</i> -LN	$\times 4$	32.57	.8997	28.91	.7887	27.76	.7426	26.79	.8063	31.41	.9188	SwinIR ₁ + <i>i</i> -LN	Test100	29.87	.8982

(a) Single image super-resolution (SR)

(b) Image deraining (DR)

Backbone	σ	Urban100		CBSD68		Kodak24		McMaster	
		PSNR	PSNR	PSNR	PSNR	PSNR	PSNR	PSNR	PSNR
HAT ₁ + LN	15	35.489	34.285	35.347	35.440				
HAT ₁ + <i>i</i> -LN	15	35.558	34.296	35.366	35.477				
SwinIR ₁ + LN	15	35.077	34.164	35.147	35.183				
SwinIR ₁ + <i>i</i> -LN	15	35.138	34.181	35.177	35.223				
HAT ₁ + LN	25	33.296	31.622	32.864	33.105				
HAT ₁ + <i>i</i> -LN	25	33.384	31.632	32.887	33.139				
SwinIR ₁ + LN	25	32.753	31.480	32.643	32.829				
SwinIR ₁ + <i>i</i> -LN	25	32.803	31.489	32.660	32.848				

(c) Color image denoising (DN)

(d) Image JPEG compression artifact removal (CAR)

ies (Lim et al., 2017b; Wang et al., 2018), where multiplying a small scale factor to the residual path components helped the network to converge. Overall, this study aims to explore 1) the feature divergence tendency of per-token and holistic normalizations and 2) determine which normalization method yields the best performance.

Feature Divergence Behavior. Fig.4 illustrates that feature divergence always emerges when using per-token normalizations: vanilla LN, RMSNorm, and LayerScale. In contrast, spatially consistent normalizations as our *i*-LN or BN, IN, ReZero do not exhibit the divergence trend. For the configuration without any normalization, we observe failure to converge due to unstable training. However, the feature magnitudes are well-bounded before this failure occurs, aligning with other normalization schemes without the per-token operation. This observation also aligns with our hypothesis that the feature divergence phenomena is closely related to the per-token normalization, and also reveals that any spatially consistent normalization could potentially reduce this effect.

Performance Comparisons. We further analyze the empirical performance for each normalization scheme in Tab.1. Conventional LN performs the worst since it neglects inter-token spatial relationships and maps features into a unified normalized space, disregarding the input-dependent feature statistics.

LayerScale and RMSNorm show improvement against vanilla LN, but perform worse than methods with spatially consistent normalization. Meanwhile, without any normalization (None), the network fails to converge potentially due to unstable gradients raised by the absence of normalization, similar to prior studies in RZ (Bachlechner et al., 2021). BN leads to a significant performance drop in eval-mode, despite being healthy in train-mode; consistent with prior studies (Lim et al., 2017b; Wang et al., 2022a). This signifies the necessity of per-image statistics within the normalization scheme for IR tasks. IN performs better than vanilla LN but worse than ours. Both IN and BN discard crucial channel-wise information necessary for representing deep features, resulting in limited performance. However, despite these limitations in current spatially holistic normalization schemes (IN, BN), they already outperform those with per-token schemes (LN, LS, RMS). Meanwhile, our *i*-LN achieves the best performance among all examined methods, demonstrating its effectiveness in preserving important inter-token spatial relationships and internal statistics, and ultimately the input low-level features throughout the network.

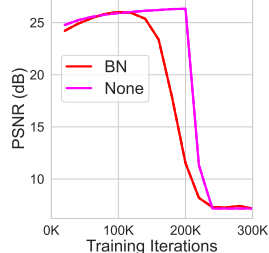


Figure 5: Eval-mode BN and removing all normalization (None) fails.

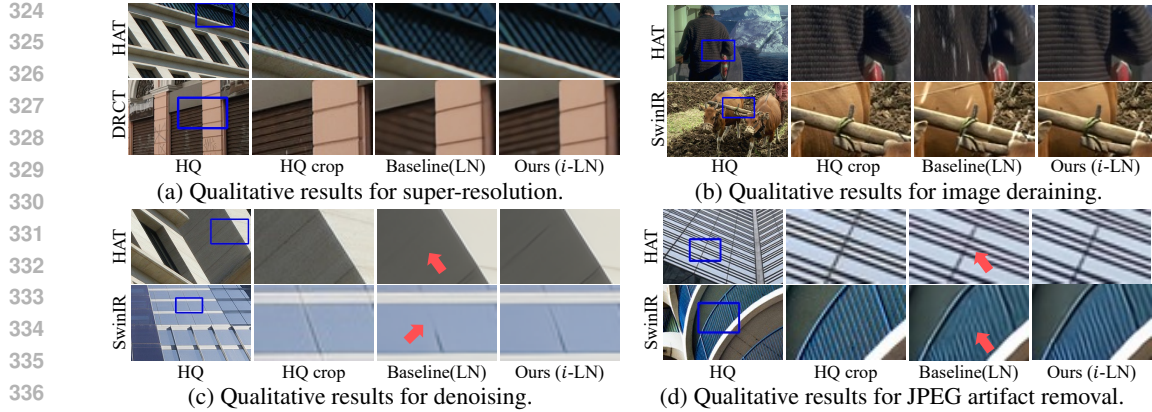


Figure 6: Qualitative comparison across four representative image restoration tasks.

3.2 ANALYSIS UNDER TASK VARIATION

Feature Divergence Behavior. Fig. 2c illustrates the evolution of feature magnitudes across various Image Restoration (IR) tasks, including Image Super-Resolution (SR), Image Denoising (DN), Image Deraining (DR), and JPEG Compression Artifact Removal (CAR). The figure clearly demonstrates that feature divergence consistently occurs across all restoration tasks under conventional LayerNorm. In contrast, integrating our *i*-LN effectively resolves this issue, maintaining stable and well-bounded feature scales throughout training. This consistent stabilization of internal feature magnitudes confirms the general applicability and robustness of our proposed method across diverse IR scenarios.

Benchmark: Image Super-Resolution (SR). Tab.2a and Fig.6a illustrate quantitative and qualitative results for SR. Compared to vanilla LayerNorm, we achieve significant improvements across benchmarks. Notably, SR benefits greatly from our method due to the inherent nature of SR: the input is entirely reliable, since it exactly aligns with the low-frequency information in the ground truth. By precisely preserving these input features, our method substantially enhances restored image quality. We additionally provide a comparison against the official public models under computationally extensive settings in Appendix.B.1.

Benchmark: Image Deraining (DR). Similarly, Tab. 2b and Fig. 6b demonstrate substantial improvements of our method in image deraining compared to conventional LayerNorm. This improvement is particularly pronounced because our method effectively preserves reliable input regions, specifically the local areas unaffected by rain streaks. By explicitly maintaining these local correspondences with the ground truth, our *i*-LN method achieves improved restoration accuracy.

Benchmark: Image Denoising (DN) Tab. 2c and Fig. 6c demonstrate that our method consistently outperforms conventional LayerNorm in image denoising tasks. However, the observed performance improvements are smaller compared to SR and Deraining. This relatively reduced benefit arises because denoising involves uniformly distributed corruptions across the entire image, limiting the advantage gained from explicitly preserving particular input features. Despite this, visual examples confirm meaningful improvements in recovering sharp edges.

Benchmark: JPEG compression artifact removal (CAR). Similarly, Tab. 2d and Fig. 6d demonstrate consistent improvements of our method over LayerNorm for JPEG compression artifact removal. However, these performance gains remain smaller than those achieved in SR and Deraining. Similar to denoising, JPEG artifacts affect images globally and irregularly, limiting the advantage of explicitly preserving specific input details. Still, visual examples illustrate consistent improvement in accurate artifact reductions, highlighting our method’s broad effectiveness across various IR tasks.

Real-world Degradation Scenarios. To further validate the effectiveness and robustness of the proposed method, we conduct further experiments under the challenging real-world degradation configurations. Here, we choose the representative Real-ESRGAN Wang et al. (2021) degradation pipeline and synthesize both the train and test images accordingly. Experiments are performed under the $\times 4$ SR task with the HAT₁ model. In Fig. 9 and Tab. 15, we provide qualitative and quantitative results, respectively. As demonstrated, our *i*-LN shows significant improvements even under the complex real-world degradation settings, successfully reconstructing fine-details and sharp edges.

378
379380 3.3 ABLATION STUDY
381

382 To analyze the contribution of each component in *i*-LN, we conduct
383 an ablation study by selectively removing spatial holisticness and
384 rescaling. Compared to Tab.2, we increase the network capacity and
385 training iterations (denoted as HAT₂) to ensure that the observed
386 benefits are not simply due to faster convergence. **In Tab. 3, Fig.13**
387 **and Fig.12, we provide a quantitative and qualitative analysis results**
388 **under the $\times 4$ SR task.** Removing either the rescaling strategy (Rs) or
389 the spatial holisticness (SH) consistently reduces restoration quality,
390 confirming their complementary roles in improving IR performance.
391

392 We then examine feature statistics in Fig. 7. Starting from our full
393 method, we remove the rescaling method (falling back to LN*) and
394 subsequently the spatial holistic scheme (falling back to vanilla per-
395 token LN). Here, we observe that channel entropy collapses *exponentially*,
396 indicating that each component contributes to maintaining
397 well-distributed activations across channels.

398 Overall, using both components together achieves the best results in terms of both restoration quality
399 and stable feature statistics. Spatial holisticness (LN*) effectively preserves inter-token relationships,
400 while the rescaling strategy further restores the missing global scale that LN* alone cannot maintain.
401

402 3.4 INTRIGUING PROPERTIES OF FEATURE DIVERGENCE UNDER VANILLA LN
403404 3.4.1 HOW NETWORK SCALE IMPACTS FEATURE DIVERGENCE
405

406 We further investigate how the overall network size affects feature divergence by varying the depth
407 and width of the IR Transformer individually. As shown in Fig. 2a–2b, larger models consistently
408 diverge faster and to higher magnitudes. In particular, the emergence of an extreme valued feature
409 appears to be a cumulative process: in order for a newly generated outlier channel to dominate the
410 statistics, it must surpass the already abnormal activations propagated through the residual path,
411 resulting in increasingly extreme values as the network scales. Taken together, our analysis reveals
412 a potential vulnerability unique to low-level restoration at scale, where enlarging capacity does not
413 merely amplify representational power but also exacerbates pathological feature growth.
414

415 3.4.2 CHANNEL IMBALANCE AND BIAS ALIGNMENT
416

417 Earlier, we observed extreme feature norms and imbalances
418 in channel entropy, indicating highly peaky feature distribu-
419 tions concentrated in specific channels. Interestingly, despite
420 these severe imbalances, baseline IR Transformers manage to
421 converge and produce outputs with well-bounded magnitudes.
422 To gain insights to this paradox, we take a closer look at the
423 final normalization layer (LN). In Fig. 8, we visualize the un-
424 normalized feature magnitudes along the channel dimension
425 before the final normalization layer and compare them with
426 the learned affine bias parameter (γ) across various IR tasks.
427

428 We observe sharp peaks in the bias parameters precisely align-
429 ing with the channels exhibiting high magnitudes. This exact alignment reveals a compensatory mech-
430 anism where the learnable affine terms (γ, β) of LayerNorm counteract abnormal channel activations,
431 allowing baselines to yield normal images. Additionally, this also indicates that the normalization
432 operation (μ, σ) itself is incapable of directly removing these extreme peaks.

433 Moreover, although the observed bias–feature alignment allows baseline IR Transformers to maintain
434 reasonable outputs, this mechanism should be regarded as a compensatory shortcut rather than a
435 fundamental fix. The fact that networks must rely on such peaky biases to counteract extreme channel
436 activations leaves the model fragile and prone to failures, including potential training instability and
437 failure in practical scenarios such as reduced-precision inference as discussed in Sec.3.5.2.

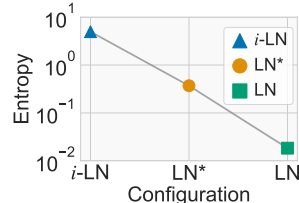


Figure 7: Channel entropy collapses *exponentially* as we remove each component (spatially holisticness and rescaling) of our *i*-LN; falling back to vanilla LN.

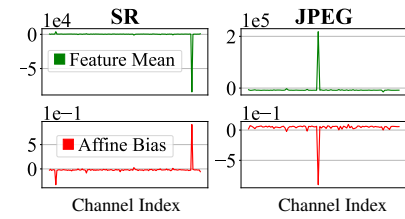


Figure 8: Alignment of affine bias parameters in the last LN and channel-
wise magnitude of input feature; showing a compensatory mechanism.

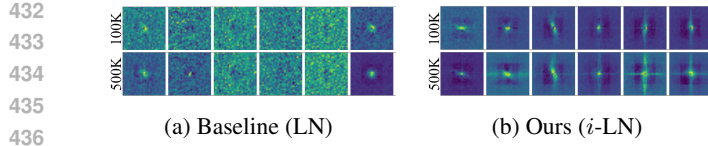


Figure 9: Visualization of Relative Position Embeddings (RPE) per head, for training iteration 100K and 500K. Ours exhibit well-structured RPEs, indicating the superiority in understanding the spatial relationship between pixels.

Idx	Backbone	SH	Rs	BSD100	Urban100	Manga109
1	HAT ₂ (LN)			27.7897	26.8779	31.5444
2	HAT ₂		✓	27.8615	27.3373	31.8888
3	HAT ₂	✓		27.9034	27.5335	32.0837
4	HAT ₂ (i-LN)	✓	✓	27.9206	27.5849	32.1694

Table 3: Ablation study. *SH* indicates introducing spatial holisticness (identical to LN*) and *Rs* indicates our rescaling strategy. *Idx 1* and *4* are each identical to vanilla LN and our *i*-LN, respectively. Experiments conducted for $\times 4$ SR.

3.5 INTRIGUING PROPERTIES UNDER *i*-LN

3.5.1 ENHANCED SPATIAL CORRELATION VIA STRUCTURED RPE

Relative Position Embeddings (RPE) explicitly encodes relative spatial positions between tokens in an input-agnostic manner, similar to the convolution operation that inherently captures the spatial locality through their structured kernel patterns. Accordingly, we can consider well-structured RPEs as a strong indicator of enhanced spatial correlation understanding. In Fig.9, we analyze how our proposed normalization method influences spatial relationship modeling by visualizing the learned RPE of both the baseline IR Transformer and our proposed method. The baseline Transformer exhibits noisy, unstructured embedding patterns, suggesting a limited capability to effectively model spatial correlations. Conversely, our method produces RPEs that resemble well-structured convolutional filter patterns, clearly indicating superior capture of spatial relationships. This structured embedding aligns with our hypothesis that our spatially holistic normalization better preserves intrinsic spatial correlations, helping the network to learn spatial relations more effectively. [In Fig. 12, we provide further visual examples of RPEs between LN, *i*-LN and also the ablated variants LN* and LN+Rescaling, which shows aligning results with the discussion above.](#)

3.5.2 LOW PRECISION INFERENCE

Image restoration networks often require deployment on lightweight edge devices, creating significant demand for efficient inference in IR Transformers. A common approach to enhance inference efficiency is reducing precision during model deployment. Consequently, we conducted experiments under reduced-precision inference conditions to empirically evaluate the effects of *i*-LN. Initially, we applied linear weight quantization to the model weights. As shown in Tab.4, vanilla LayerNorm resulted in substantial performance degradation, while *i*-LN demonstrated remarkable stability. We further conducted half-precision inference experiments, casting both internal feature values and weights to half-precision floating-point numbers. Fig.10 illustrates that vanilla LayerNorm generated extensive regions of black dots, indicating network-generated infinity values due to extreme internal feature magnitudes inadequate for low-precision conditions. Notably, no substantial performance degradation was observed in regions where the network maintained finite feature values. This highlights the necessity of well-bounded feature values achieved by *i*-LN, emphasizing its critical role in enabling efficient inference for IR Transformers.

3.5.3 EMPIRICAL EFFECTS OF IMPROVED STABILITY

Multiple Runs. To further probe training stability, we conduct extensive multi-run experiments across diverse random seeds (Fig.11). Here, we use a small batch size of 2 to induce training instability. Vanilla LN exhibits inconsistent optimization trajectories, with large fluctuations in feature statistic evolution patterns and substantial discrepancy in final PSNR results for each run. In contrast, our *i*-LN produces significantly lower variance between multiple runs, in terms of both training statistics and

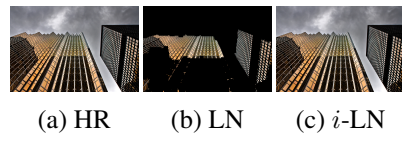


Figure 10: Half-precision inference results for $\times 4$ SR. LN leads to artifacts while our *i*-LN achieves near-zero fidelity loss compared to full-precision.

Idx	Backbone	Quantization	Urban100	Manga109
1	HAT ₂ + LN	W	int8	26.8711
2	HAT ₂ + <i>i</i> -LN	W	int8	27.5818
3	HAT ₂ + LN	W	int4	25.0242
4	HAT ₂ + <i>i</i> -LN	W	int4	26.8292
5	HAT ₂ + LN	W+F	fp16	7.4640
6	HAT ₂ + <i>i</i> -LN	W+F	fp16	27.5849
				32.1693

Table 4: Quantitative results under low-precision inference. *W* indicates weight-only quantization, *W+F* indicates weight and feature quantization.

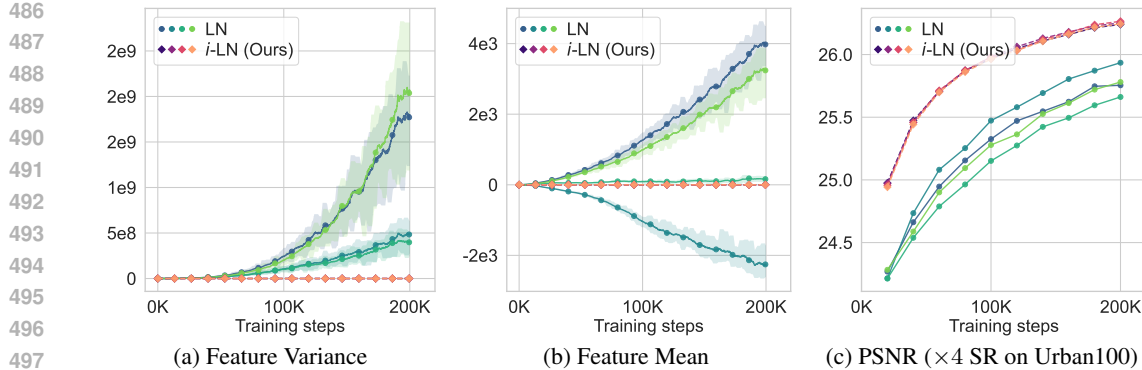


Figure 11: **Feature statistics and PSNR across multiple runs with different random seeds.** Trajectories show significant fluctuation under vanilla LN, while our *i*-LN maintains well-bounded and consistent results across all seeds ($\times 4$ SR, Urban100).

the final reconstruction performance. These results demonstrate that *i*-LN provides a more reliable optimization landscape, reducing susceptibility to randomness in initialization or data ordering, which is an important practical advantage for training IR networks.

4 RELATED WORK

Image Restoration Transformers. Recent advances in Image Restoration (IR) transformers (Chen et al., 2024; Zamir et al., 2022; Wang et al., 2022c; Zhang et al., 2022) show superior performance over CNNs (Dong et al., 2015; Kim et al., 2016; Zhang et al., 2018) by leveraging attention mechanisms to effectively model long-range context. A pioneering work, SwinIR (Liang et al., 2021), adopted an efficient Swin-Transformer (Liu et al., 2021) based architecture in IR tasks, balancing computational cost and restoration quality. A notable method is HAT, which originated as a super-resolution model (Chen et al., 2023b) but expanded to general image restoration tasks (Chen et al., 2023a). By unifying spatial and channel attention within a hybrid attention framework, HAT surpasses existing IR Transformers in both restoration fidelity and robustness across various IR tasks.

Abnormal Feature Behaviors. Normalization is a key element in enhancing stability and performance in deep networks, but also can lead to unintended feature behavior. EDSR (Lim et al., 2017b), which is a foundational work in super-resolution pointed out that BatchNorm removes range flexibility of intermediate features, leading to a performance drop. Accordingly, normalization layers are removed in the most recent CNN-based SR architectures. Meanwhile, ESRGAN (Wang et al., 2018) and StyleGAN2 (Karras et al., 2020) observe that InstanceNorm and BatchNorm, respectively, cause water droplet-like artifacts. They suggest that the generator might learn to deceive feature statistics by sneaking abnormal values in internal features to reduce the effects of normalization. EDM2 (Karras et al., 2024) identifies feature magnitude divergence in diffusion models. Accordingly, they redesign the network architecture to preserve the magnitude based on statistical assumptions, leading to overall performance enhancement. DRCT (Hsu et al., 2024) notes that feature map intensities drop sharply at the end of SR networks, leading to information bottlenecks, and shows that dense residuals help.

5 CONCLUSION

We analyzed the training dynamics of Image Restoration (IR) Transformers and highlighted an overlooked phenomenon: divergence of feature magnitudes accompanied by collapses in channel-wise entropy. We interpret this as networks attempting to bypass the constraints of conventional LayerNorm, whose per-token normalization and input-independent scaling disrupt spatial correlations and restrict the flexibility needed for accurate restoration. To address this, we introduced Image Restoration Transformer Tailored Layer Normalization (*i*-LN), a simple drop-in replacement for LayerNorm. It is designed to better align with the unique characteristics of IR tasks and preserve important low-level features of the input throughout the network. *i*-LN normalizes jointly across spatial and channel dimensions and incorporates input-dependent rescaling, aligning normalization more closely with the demands of IR tasks. Extensive experiments show that *i*-LN prevents feature divergence, stabilizes channel entropy, improves robustness under low-precision inference, and significantly enhances IR performance across diverse tasks.

540 6 REPRODUCIBILITY STATEMENT

542 Experimental settings for both training and evaluation are described in Sec.3. Detailed hyperparameter
 543 settings and network configurations for each model variant are described in Appendix.B.1 and Tab.5.
 544 Detailed algorithm to calculate the channel entropy is in Appendix.A.2 We plan to release the code
 545 for further reproducibility.

547 REFERENCES

549 Eirikur Agustsson and Radu Timofte. Ntire 2017 challenge on single image super-resolution: Dataset
 550 and study. In *Proceedings of the IEEE Conference on Computer Vision and Pattern Recognition*
 551 Workshops, pp. 126–135, 2017.

552 Jimmy Lei Ba, Jamie Ryan Kiros, and Geoffrey E Hinton. Layer normalization. *arXiv preprint*
 553 *arXiv:1607.06450*, 2016.

555 Thomas Bachlechner, Bodhisattwa Prasad Majumder, Henry Mao, Gary Cottrell, and Julian McAuley.
 556 Rezero is all you need: Fast convergence at large depth. In *Uncertainty in Artificial Intelligence*,
 557 pp. 1352–1361. PMLR, 2021.

558 Marco Bevilacqua, Aline Roumy, Christine Guillemot, and Marie Line Alberi-Morel. Low-complexity
 559 single-image super-resolution based on nonnegative neighbor embedding. 2012.

561 Yochai Blau and Tomer Michaeli. Rethinking lossy compression: The rate-distortion-perception
 562 tradeoff. In *International Conference on Machine Learning*, pp. 675–685. PMLR, 2019.

563 Rob Brekelmans, Daniel Moyer, Aram Galstyan, and Greg Ver Steeg. Exact rate-distortion in
 564 autoencoders via echo noise. *Advances in neural information processing systems*, 32, 2019.

565 Xiangyu Chen, Xintao Wang, Wenlong Zhang, Xiangtao Kong, Yu Qiao, Jiantao Zhou, and Chao
 566 Dong. Hat: Hybrid attention transformer for image restoration. *arXiv preprint arXiv:2309.05239*,
 567 2023a.

569 Xiangyu Chen, Xintao Wang, Jiantao Zhou, Yu Qiao, and Chao Dong. Activating more pixels in
 570 image super-resolution transformer. In *Proceedings of the IEEE/CVF conference on computer*
 571 *vision and pattern recognition*, pp. 22367–22377, 2023b.

572 Xiangyu Chen, Zheyuan Li, Yuandong Pu, Yihao Liu, Jiantao Zhou, Yu Qiao, and Chao Dong.
 573 A comparative study of image restoration networks for general backbone network design. In
 574 *European Conference on Computer Vision*, pp. 74–91. Springer, 2024.

576 Chao Dong, Chen Change Loy, Kaiming He, and Xiaoou Tang. Image super-resolution using deep
 577 convolutional networks. *IEEE transactions on pattern analysis and machine intelligence*, 38(2):
 578 295–307, 2015.

579 Alexey Dosovitskiy, Lucas Beyer, Alexander Kolesnikov, Dirk Weissenborn, Xiaohua Zhai, Thomas
 580 Unterthiner, Mostafa Dehghani, Matthias Minderer, Georg Heigold, Sylvain Gelly, et al. An
 581 image is worth 16x16 words: Transformers for image recognition at scale. *arXiv preprint*
 582 *arXiv:2010.11929*, 2020.

584 Alessandro Foi, Vladimir Katkovnik, and Karen Egiazarian. Pointwise shape-adaptive dct for high-
 585 quality denoising and deblocking of grayscale and color images. *IEEE transactions on image*
 586 *processing*, 16(5):1395–1411, 2007.

587 R. Franzen. Kodak lossless true color image suite. <http://r0k.us/graphics/kodak>, 1999.
 588 Volume 4, no. 2.

589 Irina Higgins, Loic Matthey, Arka Pal, Christopher Burgess, Xavier Glorot, Matthew Botvinick,
 590 Shakir Mohamed, and Alexander Lerchner. beta-vae: Learning basic visual concepts with a
 591 constrained variational framework. In *International conference on learning representations*, 2017.

593 Chih-Chung Hsu, Chia-Ming Lee, and Yi-Shiuan Chou. Drct: Saving image super-resolution away
 594 from information bottleneck. *arXiv preprint arXiv:2404.00722*, 2024.

594 Jia-Bin Huang, Abhishek Singh, and Narendra Ahuja. Single image super-resolution from transformed
 595 self-exemplars. In *Proceedings of the IEEE conference on computer vision and pattern recognition*,
 596 pp. 5197–5206, 2015.

597

598 Sergey Ioffe and Christian Szegedy. Batch normalization: Accelerating deep network training by
 599 reducing internal covariate shift. In *International conference on machine learning*, pp. 448–456.
 600 pmlr, 2015.

601

602 Kui Jiang, Zhongyuan Wang, Peng Yi, Chen Chen, Baojin Huang, Yimin Luo, Jiayi Ma, and Junjun
 603 Jiang. Multi-scale progressive fusion network for single image deraining. In *Proceedings of the
 604 IEEE/CVF conference on computer vision and pattern recognition*, pp. 8346–8355, 2020.

605

606 Tero Karras, Samuli Laine, Miika Aittala, Janne Hellsten, Jaakko Lehtinen, and Timo Aila. Analyzing
 607 and improving the image quality of stylegan. In *Proceedings of the IEEE/CVF conference on
 608 computer vision and pattern recognition*, pp. 8110–8119, 2020.

609

610 Tero Karras, Miika Aittala, Jaakko Lehtinen, Janne Hellsten, Timo Aila, and Samuli Laine. Analyzing
 611 and improving the training dynamics of diffusion models. In *Proceedings of the IEEE/CVF
 612 Conference on Computer Vision and Pattern Recognition*, pp. 24174–24184, 2024.

613

614 Jiwon Kim, Jung Kwon Lee, and Kyoung Mu Lee. Accurate image super-resolution using very deep
 615 convolutional networks. In *Proceedings of the IEEE conference on computer vision and pattern
 616 recognition*, pp. 1646–1654, 2016.

617

618 Jingyun Liang, Jie Zhang Cao, Guolei Sun, Kai Zhang, Luc Van Gool, and Radu Timofte. Swinir: Im-
 619 age restoration using swin transformer. In *Proceedings of the IEEE/CVF International Conference
 620 on Computer Vision*, pp. 1833–1844, 2021.

621

622 Bee Lim, Sanghyun Son, Heewon Kim, Seungjun Nah, and Kyoung Mu Lee. Enhanced deep residual
 623 networks for single image super-resolution. In *The IEEE Conference on Computer Vision and
 624 Pattern Recognition (CVPR) Workshops*, July 2017a.

625

626 Bee Lim, Sanghyun Son, Heewon Kim, Seungjun Nah, and Kyoung Mu Lee. Enhanced deep residual
 627 networks for single image super-resolution. In *Proceedings of the IEEE conference on computer
 628 vision and pattern recognition workshops*, pp. 136–144, 2017b.

629

630 Ze Liu, Yutong Lin, Yue Cao, Han Hu, Yixuan Wei, Zheng Zhang, Stephen Lin, and Baining Guo.
 631 Swin transformer: Hierarchical vision transformer using shifted windows. In *Proceedings of the
 632 IEEE/CVF international conference on computer vision*, pp. 10012–10022, 2021.

633

634 David Martin, Charless Fowlkes, Doron Tal, and Jitendra Malik. A database of human segmented
 635 natural images and its application to evaluating segmentation algorithms and measuring ecological
 636 statistics. In *Proceedings Eighth IEEE International Conference on Computer Vision. ICCV 2001*,
 volume 2, pp. 416–423. IEEE, 2001.

637

638 Yusuke Matsui, Kota Ito, Yuji Aramaki, Azuma Fujimoto, Toru Ogawa, Toshihiko Yamasaki, and
 639 Kiyoharu Aizawa. Sketch-based manga retrieval using manga109 dataset. *Multimedia Tools and
 640 Applications*, 76:21811–21838, 2017.

641

642 H Sheikh. Live image quality assessment database release 2. <http://live.ece.utexas.edu/research/quality>, 2005.

643

644 Hugo Touvron, Matthieu Cord, Alexandre Sablayrolles, Gabriel Synnaeve, and Hervé Jégou. Going
 645 deeper with image transformers. In *Proceedings of the IEEE/CVF international conference on
 646 computer vision*, pp. 32–42, 2021.

647

648 Dmitry Ulyanov, Andrea Vedaldi, and Victor Lempitsky. Instance normalization: The missing
 649 ingredient for fast stylization. *arXiv preprint arXiv:1607.08022*, 2016.

650

651 Xintao Wang, Ke Yu, Shixiang Wu, Jinjin Gu, Yihao Liu, Chao Dong, Yu Qiao, and Chen Change Loy.
 652 Esrgan: Enhanced super-resolution generative adversarial networks. In *Proceedings of the European
 653 conference on computer vision (ECCV) workshops*, pp. 0–0, 2018.

648 Xintao Wang, Liangbin Xie, Chao Dong, and Ying Shan. Real-esrgan: Training real-world blind super-
 649 resolution with pure synthetic data. In *Proceedings of the IEEE/CVF International Conference on*
 650 *Computer Vision*, pp. 1905–1914, 2021.

651 Xintao Wang, Chao Dong, and Ying Shan. Repsr: Training efficient vgg-style super-resolution
 652 networks with structural re-parameterization and batch normalization. In *Proceedings of the 30th*
 653 *acm international conference on multimedia*, pp. 2556–2564, 2022a.

654 Xintao Wang, Liangbin Xie, Ke Yu, Kelvin C.K. Chan, Chen Change Loy, and Chao Dong. BasicSR:
 655 Open source image and video restoration toolbox. [https://github.com/XPixelGroup/](https://github.com/XPixelGroup/BasicSR)
 656 BasicSR, 2022b.

657 Zhendong Wang, Xiaodong Cun, Jianmin Bao, Wengang Zhou, Jianzhuang Liu, and Houqiang Li.
 658 Uformer: A general u-shaped transformer for image restoration. In *Proceedings of the IEEE/CVF*
 659 *conference on computer vision and pattern recognition*, pp. 17683–17693, 2022c.

660 Wenhao Yang, Robby T Tan, Jiashi Feng, Jiaying Liu, Zongming Guo, and Shuicheng Yan. Deep
 661 joint rain detection and removal from a single image. In *Proceedings of the IEEE conference on*
 662 *computer vision and pattern recognition*, pp. 1357–1366, 2017.

663 Jingfeng Yao, Bin Yang, and Xinggang Wang. Reconstruction vs. generation: Taming optimization
 664 dilemma in latent diffusion models. In *Proceedings of the Computer Vision and Pattern Recognition*
 665 *Conference*, pp. 15703–15712, 2025.

666 Syed Waqas Zamir, Aditya Arora, Salman Khan, Munawar Hayat, Fahad Shahbaz Khan, and Ming-
 667 Hsuan Yang. Restormer: Efficient transformer for high-resolution image restoration. In *Proceedings*
 668 *of the IEEE/CVF conference on computer vision and pattern recognition*, pp. 5728–5739, 2022.

669 Roman Zeyde, Michael Elad, and Matan Protter. On single image scale-up using sparse-
 670 representations. In *International conference on curves and surfaces*, pp. 711–730. Springer,
 671 2010.

672 Biao Zhang and Rico Sennrich. Root mean square layer normalization. *Advances in Neural*
 673 *Information Processing Systems*, 32, 2019.

674 Dafeng Zhang, Feiyu Huang, Shizhuo Liu, Xiaobing Wang, and Zhezhu Jin. Swinfir: Revisiting
 675 the swinir with fast fourier convolution and improved training for image super-resolution. *arXiv*
 676 *preprint arXiv:2208.11247*, 2022.

677 He Zhang, Vishwanath Sindagi, and Vishal M Patel. Image de-raining using a conditional generative
 678 adversarial network. *IEEE transactions on circuits and systems for video technology*, 30(11):
 679 3943–3956, 2019.

680 Lei Zhang, Xiaolin Wu, Antoni Buades, and Xin Li. Color demosaicking by local directional
 681 interpolation and nonlocal adaptive thresholding. *Journal of Electronic Imaging*, 20(2):023016–
 682 023016, 2011.

683 Yulun Zhang, Kunpeng Li, Kai Li, Lichen Wang, Bineng Zhong, and Yun Fu. Image super-resolution
 684 using very deep residual channel attention networks. In *Proceedings of the European conference*
 685 *on computer vision (ECCV)*, pp. 286–301, 2018.

686 Yupeng Zhou, Zhen Li, Chun-Le Guo, Song Bai, Ming-Ming Cheng, and Qibin Hou. Srformer:
 687 Permuted self-attention for single image super-resolution. In *Proceedings of the IEEE/CVF*
 688 *international conference on computer vision*, pp. 12780–12791, 2023.

689
 690
 691
 692
 693
 694
 695
 696
 697
 698
 699
 700
 701

702 Table 5: Overview of model variants. ▶ indicates the group (type) of each model variant: from
 703 lightweight to computationally extensive settings. The according placements of the experiments
 704 are specified as *Main* (i.e., the main article) and *Appendix*. The placements of the detailed network
 705 hyperparameters and training configurations for each variant are highlighted in **bold**.
 706

707 Variant	708 Description
▶ Type1 (Lightweight Computational Configuration)	
710 SwinIR₁ - Main	711 These configurations are used for most analyses. All models were trained from scratch without the 712 Warm-start strategy (i.e., the $\times 4$ SR models are not finetuned from the $\times 2$ SR weights), Mixing 713 Augmentations, Progressive Patch Sizing.
714 DRCT₁ - Main	715 Details are provided in Tab. 10 . This variant shares the same 716 network architecture as the official SwinIR-light model imple- 717 mentation.
718 HAT₁ - Main & Appendix	719 Details are provided in Tab. 11 . This variant is a lightweight 720 variant of the DRCT Hsu et al. (2024) model implementation. 721 The embedding dimension is reduced in order align the network 722 architecture with the HAT ₁ model.
723 SRFormer₁ - Appendix	724 Details are provided in Tab. 13 . This is a variant is a lighter 725 version of the HAT-S Chen et al. (2023b) model, modified 726 with a slightly reduced embedding dimension. This change 727 was made since the standard HAT-S, despite being denoted 728 as <i>small</i> , requires more Mult-Adds than the full-sized SwinIR 729 model.
▶ Type2 (Moderate Computational Configuration)	
730 HAT₂ - Main	731 These configurations are used for the ablation study and low-precision inference analysis.
732	733 Details are provided in Tab. 14 . This variant shares the same 734 network capacity as the official HAT-S implementation, which 735 is slightly heavier than HAT ₁ . However, the training budget is 736 reduced for computational efficiency compared to HAT-S [†] (the 737 public model); the patch size and the batch size were halved 738 each. Aligning with Type1 configurations, all models were 739 trained from scratch without the warm-start strategy for 300K.
▶ Type3 (Extensive Computational Configuration)	
740 HAT[†] - Main & Appendix	741 These configurations are used when comparing with official public models and validating the 742 scalability of our method.
743	744 Details are provided in Tab. 15 . This variant shares the same 745 network architecture as the official full-sized HAT implemen- 746 tation and precisely follows the training configuration of the 747 public model. Quantitative results from this variant are copied 748 from the original paper Chen et al. (2023b).
749	750
751	752
753	754
754	755

756
 757 Table 6: Quantitative results for classical image super-resolution under **computationally extensive**
 758 setting. \dagger indicates that we have precisely followed the architecture and training settings of the **official**
 759 **public model**, as specified in Tab.15. HAT \dagger requires 40 GPU days for $\times 2$ SR (500K train iterations)
 760 and additional 20 GPU days for $\times 4$ SR (250K finetuning iterations). The best results for each setting
 761 are highlighted in **bold**, respectively.

Backbone	Scale	Set5		Set14		BSD100		Urban100		Manga109	
		PSNR	SSIM								
HAT \dagger + LN	$\times 2$	38.63	.9630	34.86	.9274	32.62	.9053	34.45	.9466	40.26	.9809
HAT \dagger + <i>i</i> -LN (Ours)	$\times 2$	38.65	.9631	34.92	.8276	32.63	.9053	34.60	.9476	40.38	.9811
HAT \dagger + LN	$\times 4$	33.04	.9056	29.23	.7973	28.00	.7517	27.97	.8368	32.48	.9292
HAT \dagger + <i>i</i> -LN (Ours)	$\times 4$	33.12	.9064	29.26	.7981	28.00	.7520	28.04	.8388	32.56	.9299

A EXPERIMENTAL DETAILS

A.1 MODEL IMPLEMENTATION DETAILS

Since this work provides extensive analysis for more than 60 configurations, analyses throughout this work are performed on various settings due to computational efficiency. We provide implementation details in terms of both network architectural hyperparameters and training configuration for each model variant in Tab.5.

- **Type1 (Lightweight Setting):** These models are the lightweight variants of the original implementations. These configurations are used in Tab.1 and Tab.2, where effects of different normalization schemes and task variations are analyzed.
- **Type2 (Moderate Setting):** These model variants indicate moderate computational budget settings. They are used for the ablation study and also for the analysis in low-precision settings (Tab.3, Tab.4, Fig.10).
- **Type3 (Computationally Extensive Setting):** These model variants indicate computationally extensive settings. This configuration is used to validate the scalability of our method (Tab.6), which aligns with the official implementation of the public models.

A.2 CHANNEL ENTROPY

Algorithm 1 represents a simple pseudocode to calculate the channel-axis entropy used in our analysis. A sharp drop in channel-axis entropy indicates that feature activations are becoming concentrated in a few specific channels. Analysis throughout this work shows that this entropy collapse is intrinsically linked to the feature divergence problem that arises from conventional LayerNorm in Image Restoration (IR) Transformers.

Algorithm 1 Channel Entropy Calculation

Require: Activation tensor x of shape (C, H, W), a small constant ϵ for numerical stability.

Ensure: A single scalar entropy value.

- ▶ Step 1: Average the total activation magnitude over spatial-dim.
- ▶ Step 2: Convert to a probability distribution.
- ▶ Step 3: Compute channel entropy.

```

1: function CHANNELENTROPY( $x, \epsilon$ )
2:    $x_{\text{avg}} \leftarrow \text{mean}(\text{abs}(x), \text{dims} = (H, W))$  ▷ Step 1
3:    $p \leftarrow \text{softmax}(x_{\text{avg}})$  ▷ Step 2
4:    $\text{entropy} \leftarrow -1 \cdot \sum(p \cdot \log(p + \epsilon))$  ▷ Step 3
5:   return  $\text{entropy}$ 
6: end function

```

810
811
812
813
814 Table 7: Quantitative results for $\times 4$ super-resolution on the SRFormer (Zhou et al., 2023) network
815 architecture. The network capacity and the training budget are adjusted as in Tab.12, which aligns with
816 experimental settings in Tab.2. The best results for each setting are highlighted in **bold**, respectively.
817

Backbone	Scale	Set5		Set14		BSD100		Urban100		Manga109	
		PSNR	SSIM								
SRFormer ₁ + LN	$\times 4$	32.41	.8972	28.77	.7853	27.68	.7398	26.43	.7957	30.98	.9141
SRFormer ₁ + <i>i</i> -LN (Ours)	$\times 4$	32.45	.8979	28.81	.7862	27.70	.7407	26.49	.7997	31.10	.9152

818
819
820
821
822
823
824
825 Table 8: Quantitative results for $\times 4$ super-resolution with additional regularization methods. *GC*
826 denotes Gradient Clipping, and *KLD* denotes an auxiliary KL-Divergence loss. Neither proved
827 effective at addressing the instability caused by LayerNorm. *GC* slightly improves stability but still
828 allows extreme feature magnitudes (5.6×10^6), comparable to the vanilla baseline (5.8×10^6). *KLD*
829 regularization enforces smoother statistics but leads to a notable performance drop. In contrast, our
830 proposed *i*-LN yields magnitudes close to $\mathcal{N}(0, 1)$ (around 1.2) while consistently outperforming all
831 alternatives. The best results for each setting are highlighted in **bold**.
832

Backbone	Scale	Set5		Set14		BSD100		Urban100		Manga109	
		PSNR	SSIM								
HAT ₁ + LN	$\times 4$	32.51	.8992	28.79	.7876	27.68	.7411	26.55	.8015	31.01	.9150
HAT ₁ + LN + <i>GC</i>	$\times 4$	32.55	.8996	28.87	.7882	27.74	.7417	26.70	.8037	31.31	.9169
HAT ₁ + LN + <i>KLD</i>	$\times 4$	32.36	.8974	28.65	.7853	27.64	.7402	26.34	.7972	30.41	.9105
HAT ₁ + <i>i</i> -LN (Ours)	$\times 4$	32.72	.9019	29.01	.7915	27.84	.7456	27.17	.8167	31.82	.9228

833 B ADDITIONAL BENCHMARK RESULTS

834 B.1 SCALING MODELS AND COMAPRISON AGAINST PUBLIC MODELS

835 In Tab.6, we validate the scalability of the proposed *i*-LN under computationally extensive settings.
836 Specifically, we train our models on top of the full-sized HAT architecture variant, with the exact
837 training configurations of the public model as specified in Tab.15. The models are indicated as HAT[†],
838 where [†] means that we have precisely followed the exact network architecture hyperparameters and
839 training configurations for fair comparison. HAT[†] for $\times 2$ SR and $\times 4$ SR variants requires 40 GPU
840 days and 20 GPU days on wall-clock time each, with NVIDIA RTX A6000s under the representative
841 BasicSR (Wang et al., 2022b) framework.
842

843 **Benchmark.** In Tab.6 we validate that replacing the conventional LayerNorm with the proposed *i*-LN
844 leads to significant performance gain also in the computationally extensive setting where the networks
845 have significantly larger capacity Accordingly, we conclude that the proposed *i*-LN is effective in
846 both 1) lightweight settings, as shown in our main article and 2) also in computationally extensive
847 settings as in Tab.6, showing the scalability of our *i*-LN.
848

849 **Training Details.** Scores are from the original paper for the baselines. Here, we follow the original
850 training scheme where $\times 4$ SR models are trained under warm-start configuration (i.e., finetuned from
851 $\times 2$ SR model weight).
852

853 B.2 ADAPTATION TO EFFICIENT SR NETWORK

854 In Tab.7, we further validate the effectiveness on top of the SRFormer Zhou et al. (2023) architecture, a
855 representative efficient SR network. Similar to other Type1 model variants, the training configurations
856 are adjusted. Refer to Tab.12 for the detailed configurations.
857

858 **Discussion.** SRFormer utilizes a Permuted Self-Attention (PSA) mechanism. Accordingly, features
859 across multiple pixels are reshaped into a single feature-pixel (pixelshuffle-style). Thus, the per-
860 token vanilla LN implicitly takes normalization parameters across multi-pixels. While the effect
861 of permuted self-attention in the perspectives of normalization was not discussed in the original
862 work, our work suggests insights that PSA induces (partially) spatial holisticaess in normalization, a
863 potential factor for the performance gain of SRFormer (i.e., potentially reducing the performance
864 gap against ours). Seeking further improvements regarding the relationship between the reshaping
865 operation and normalization may be a valuable direction for future work.
866

864 C OTHER REGULARIZATION TECHNIQUES FOR TRAINING STABILITY
865866 Beyond our proposed i -LN, one may ask whether simpler regularization methods could mitigate the
867 training instabilities of IR Transformers. We therefore examined common strategies such as gradient
868 clipping (GC) and KL divergence (KLD) regularization in Tab.8.869 While GC is widely used to bound exploding gradients, our experiments confirmed that it does not
870 prevent the emergence of extreme feature magnitudes in IR Transformers. The maximum feature
871 magnitude observed during training with GC was 5.6×10^6 . As a reference, the maximum feature
872 magnitude for the vanilla HAT₁+LN was 5.8×10^6 . In contrary, our HAT₁+ i -LN shows 1.2, very
873 closely aligning with the expected magnitude of a random noise sampled from the normal distribution
874 $\mathcal{N}(0, 1)$, which is 1. Additionally, while GC leads to slight performance improvement against the
875 vanilla model, it consistently underperforms compared to i -LN.876 Likewise, KLD regularization can stabilize feature statistics, but at the cost of substantial reconstruc-
877 tion performance degradation. Specifically, we observed that although KLD encourages well-behaved
878 distributions, the resulting models suffered PSNR drops even below the baseline with vanilla LN. This
879 is consistent with prior findings in rate-distortion theory (Brekelmans et al., 2019; Blau & Michaeli,
880 2019), and also to VAE literature (Higgins et al., 2017; Yao et al., 2025), where strong regularization
881 penalties reduce reconstruction fidelity.882 Overall, these results highlight that although general-purpose regularization may offer partial reme-
883 dies, they are either ineffective (GC) or detrimental to reconstruction quality (KLD). This further
884 emphasizes the necessity of normalization methods tailored to the unique requirements of IR Trans-
885 formers.886
887
888
889
890
891
892
893
894
895
896
897
898
899
900
901
902
903
904
905
906
907
908
909
910
911
912
913
914
915
916
917

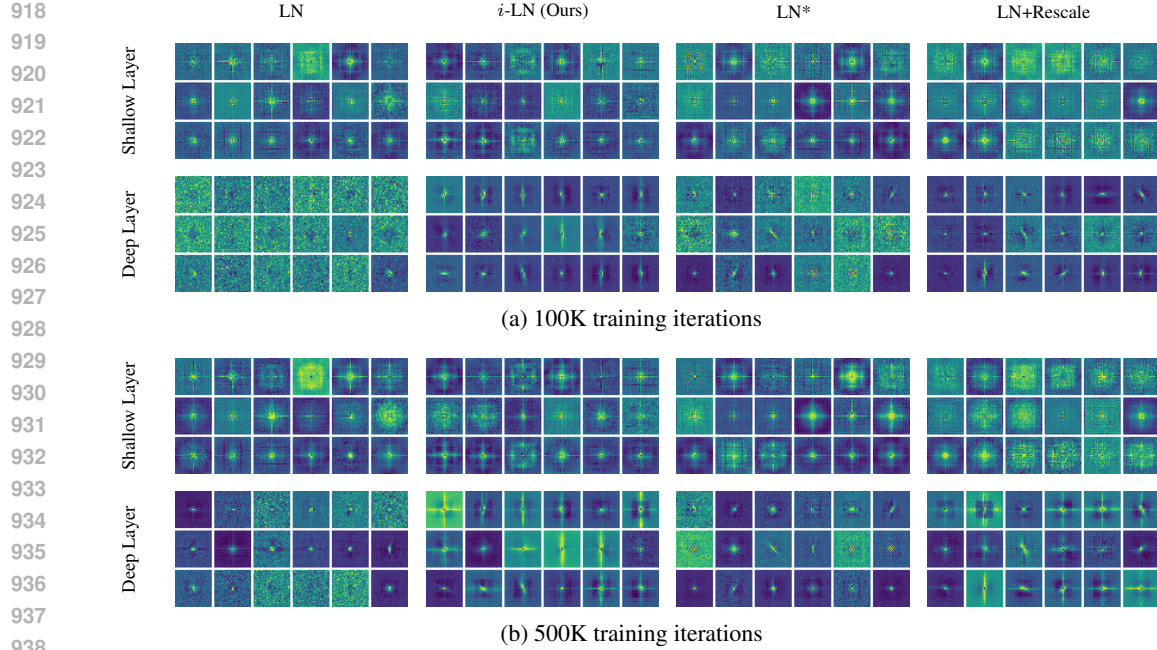


Figure 12: Visual comparison of Relative Position Embeddings (RPE) across attention heads. We show the RPEs from the last three attention layers of each a shallow (RHAG .0) and a deep (RHAG .5) building block of HAT Chen et al. (2023a) (i.e., the RHAG Block), as well as early training (100K iterations) versus fully converged models (500K iterations). Each corresponds to an experimental setting aligned with Tab. 3, where vanilla LN and our i -LN are the primary comparison, and LN* and LN+Rescale represent ablation variants obtained by selectively removing components of our method. Our full method (i -LN) yields cleaner and more stable RPE patterns, with substantially reduced noise across variations in training iteration and layer depth.

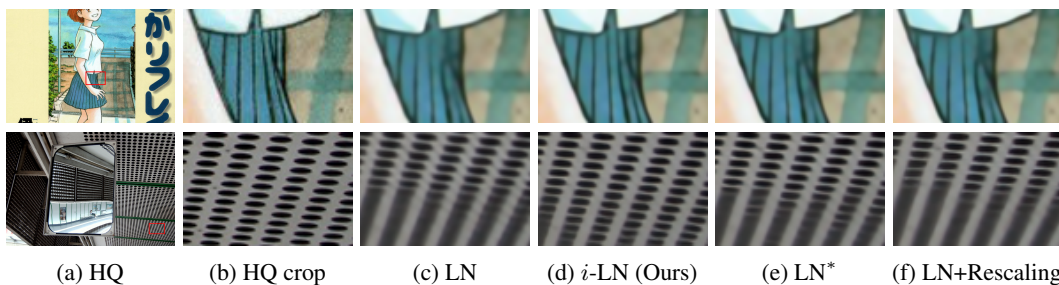


Figure 13: Visual comparison between LN and i -LN, along with the ablated variants LN* and LN+Rescaling with the HAT₂ configuration. Experimental settings follow the ablation study in the main article (Tab. 3). The proposed i -LN more faithfully reconstructs fine details, producing sharper edges and clearer complex patterns than the LN baseline.

D FURTHER ABLATION STUDY

Here, we further compare our full method *i*-LN against the baseline (vanilla) LN, and two variants: LN* and LN+Rescaling, which each are ablations of our method without rescaling (LN*) and without the spatial holistic type of normalization (LN+Rescaling). Below, we provide additional visualization of relative position embeddings (RPEs) and also further visual comparison of the according $\times 4$ SR result. Quantitative comparison can be seen in Tab.3 of the main article. Each of these experimental setups is directly aligned with the ablation analysis presented in Tab. 3 of the main article. Accordingly, all experiments were performed with the HAT₂ configuration for the synthetic (bicubic) $\times 4$ SR task.

972 D.1 ABLATION STUDY: RELATIVE POSITION EMBEDDINGS (RPE) VISUALIZATION
973974 In Fig. 12, we provide a comprehensive visual comparison of the learned Relative Position Embed-
975 dings (RPE) across different normalization strategies. The figure compares vanilla Layer Normaliza-
976 tion (LN), our proposed *i*-LN, as well as two ablated variants, LN* and LN+Rescaling.977 To obtain deeper insight into the dynamics and stability of RPE formation, we visualize both early-
978 stage training (100K iterations) and fully converged models (500K iterations), and further examine
979 representations from a shallow block (RHAG. 0) and a deep block (RHAG. 5).980 Across all settings, vanilla LN exhibits highly noisy RPE structures throughout the entire training
981 process. Even after convergence, its embeddings fail to organize into meaningful spatial patterns,
982 suggesting a limited ability to encode coherent spatial correlations. The LN* variant, which adopts a
983 spatially holistic normalization, occasionally reveals global structures, but these patterns remain weak
984 and are overshadowed by considerable noise. The LN+Rescaling variant shows improved structure in
985 deeper layers, yet its shallow-layer embeddings remain unstable and inconsistent. This indicating
986 that rescaling alone is insufficient to guide early-layer RPE formation, reflected in low reconstruciton
987 scores in Tab.3.988 In contrast, our proposed *i*-LN consistently produces substantially clearer and more structured
989 RPE maps, with significantly reduced noise across both shallow and deep layers and across all
990 training stages. The strong spatial coherence visible in the embeddings aligns with the quantitative
991 improvements reported in Tab. 3, where *i*-LN achieves the highest performance among all evaluated
992 variants. These visual results confirm that *i*-LN facilitates stable and meaningful spatial relational
993 modeling throughout the entire network depth and training trajectory.995 D.2 ABLATION STUDY: $\times 4$ SR VISUALIZATION
996997 In Fig.13, we provide additional visual comparisons between the SR outputs obtained by networks
998 each employing LN, LN*, LN+Rescale and our *i*-LN.999 Across all cases, the model equipped with *i*-LN produces the sharpest and most faithful reconstruction
1000 of fine-grained structures, including thin edges, repetitive patterns, and high-frequency textures. The
1001 restored images exhibit not only improved clarity but also enhanced local contrast and reduced
1002 artificial smoothing, indicating that *i*-LN effectively preserves low-level feature statistics throughout
1003 the network.1004 By contrast, the baseline vanilla LN often yields blurry and overly smoothed outputs, where crucial
1005 high-frequency details are lost. This degradation is consistent with the unstable and noisy RPE
1006 behavior observed earlier, suggesting that vanilla LN struggles to maintain coherent spatial relations
1007 required for accurate detail reconstruction. The ablated variants as LN* (spatial holistic normal-
1008 ization without rescaling) and LN+Rescaling (rescaling without spatial holisticness) show partial
1009 improvements over LN but still fall short of *i*-LN.1010 Overall, the qualitative comparisons provide visual evidence that both components of *i*-LN (spatial
1011 holisticness and input-adaptive rescaling) are essential.1014 E ADDITIONAL EXPERIMENTS ON THE STABILITY AND ROBUSTNESS
10151016 In this section, we provide additional experiments that further validate the stability, robustness, and
1017 general applicability of the proposed *i*-LN across a wide range of practical and challenging training
1018 scenarios. Specifically, we evaluate: 1) real-world super-resolution settings, 2) robustness under
1019 multiple training batch sizes.1020 Across all settings, *i*-LN consistently outperforms and exhibits more stable behavior than the con-
1021 ventional per-token LayerNorm (LN). Unless otherwise specified, the base configuration follows the
1022 HAT₁ setting for the $\times 4$ SR task. In all experiments, we compare against the vanilla LN baseline
1023 under identical training configurations.

1025 E.1 ROBUSTNESS ACROSS VARYING BATCH SIZES

Run	Backbone	Set5		Set14		BSD100		Urban100		Manga109		
		PSNR	SSIM	PSNR	SSIM	PSNR	SSIM	PSNR	SSIM	PSNR	SSIM	
1	RealHAT ₁ + LN	26.27	.7601	24.43	.6272	24.39	.5881	22.01	.6064	23.65	.7466	
	RealHAT ₁ + <i>i</i> -LN	26.38	.7656	24.58	.6322	24.47	.5918	22.19	.6146	23.96	.7557	
2	RealHAT ₁ + LN	26.77	.7739	24.27	.6201	24.29	.5839	22.00	.6056	23.61	.7503	
	RealHAT ₁ + <i>i</i> -LN	26.90	.7777	24.46	.6272	24.37	.5876	22.19	.6141	23.84	.7587	
3	RealHAT ₁ + LN	24.39	.6927	24.77	.6325	24.32	.5823	21.96	.5973	23.71	.7522	
	RealHAT ₁ + <i>i</i> -LN	24.58	.6993	24.94	.6377	24.40	.5862	22.16	.6055	23.99	.7602	
4	RealHAT ₁ + LN	25.86	.7472	24.72	.6389	24.35	.5878	21.84	.5954	23.22	.7365	
	RealHAT ₁ + <i>i</i> -LN	26.05	.7531	24.93	.6447	24.43	.5913	22.04	.6046	23.48	.7450	
5	RealHAT ₁ + LN	25.08	.7086	24.46	.6355	24.38	.5899	21.93	.6032	23.46	.7458	
	RealHAT ₁ + <i>i</i> -LN	25.26	.7120	24.63	.6411	24.46	.5933	22.10	.6115	23.73	.7554	
Avg.		RealHAT ₁ + LN	25.68	.7365	24.53	.6308	24.35	.5864	21.95	.6016	23.53	.7463
		RealHAT ₁ + <i>i</i> -LN	25.83	.7415	24.71	.6366	24.43	.5900	22.14	.6101	23.80	.7550

Table 9: Quantitative results for real-world $\times 4$ super-resolution across five random seeds. Both the training images and the test images were synthesized following the Real-ESRGAN (Wang et al., 2021) degradation pipeline. The best results for each setting are highlighted in **bold**.

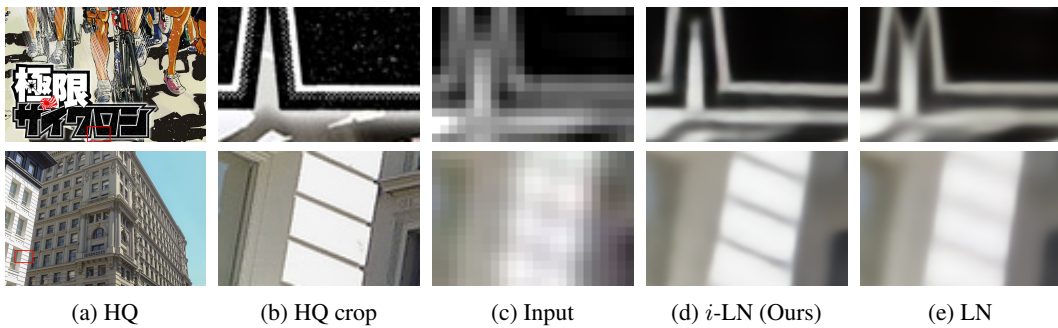


Figure 15: Visual comparison between LN and *i*-LN for the real-world $\times 4$ super-resolution task with HAT₁. Both the training images and the test images were synthesized following the Real-ESRGAN (Wang et al., 2021) degradation pipeline.

To evaluate the robustness of *i*-LN, we train HAT₁ models but with varying batch size from 2 to 8; while keeping all other hyperparameters fixed (Fig. 14). This experimental design is chosen in order to mimic unstable training configurations without heavy hyperparameter search. For each configuration, we report PSNR and SSIM for the $\times 4$ SR task on Urban100 throughout training. As shown in Fig. 14, models with *i*-LN consistently achieve higher PSNR/SSIM than the baseline across all batch sizes. Notably, the performance gap remains stable as the batch size decreases. These results demonstrate that the benefit of *i*-LN is not tied to a particular training setup, and that its stability advantages persist even under extremely small-batch training (e.g., batch size 2). This property is especially valuable for memory-constrained environments where large batches are infeasible.

E.2 REAL-WORLD SUPER-RESOLUTION

To evaluate the practical effectiveness of *i*-LN, we adopt a real-world degradation setup following the RealESRGAN Wang et al. (2021) pipeline. These analyses complement the main text by demonstrating that the advantages of *i*-LN are not restricted to controlled laboratory settings, but generalize to real-world usage and unstable training regimes.

Training is performed on synthetic DF2K pairs, and testing is conducted on synthetically degraded versions of standard SR benchmarks (Set5, Set14, BSD100, Urban100, Manga109). Degradation syn-

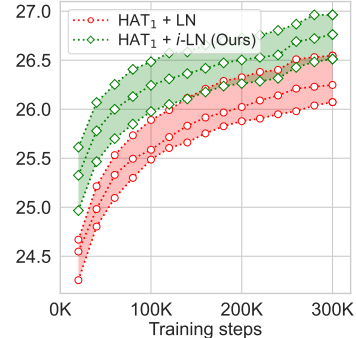


Figure 14: PSNR for $\times 4$ SR with the HAT₁ model, but with batch size 2, 4, 8 (Urban100).

1080
1081 thesis strictly follows the RealESRGAN procedures. To assess robustness, we repeat each experiment
1082 across five different random seeds and report the average score of the resulting PSNR/SSIM scores.
1083

1084 As shown in Tab.9 and Fig.15, *i*-LN leads to consistent and significant improvements over vanilla
1085 LN across all benchmarks, despite the increased complexity of the real-world degradation pipeline.
1086 These results highlight that *i*-LN is not only theoretically grounded but also practically beneficial in
1087 more challenging real-world restoration scenarios.

1088 **F ADDITIONAL QUALITATIVE COMPARISON**

1089 We provide additional visual comparisons between IR Transformers with our proposed *i*-LN against
1090 their counterparts using vanilla Layer Normalization (LN). As shown in the following figures, *i*-LN
1091 consistently produces sharper structures, cleaner textures, and fewer artifacts across a range of low-
1092 level vision tasks. Qualitative results are provided for: (i) super-resolution (Figs. 16 and 17), (ii)
1093 image denoising (Figs. 18 and 19), (iii) JPEG compression artifact removal (Figs. 23 and 22), and
1094 (iv) image deraining (Figs. 20 and 21).

1095

1096

1097

1098

1099

1100

1101

1102

1103

1104

1105

1106

1107

1108

1109

1110

1111

1112

1113

1114

1115

1116

1117

1118

1119

1120

1121

1122

1123

1124

1125

1126

1127

1128

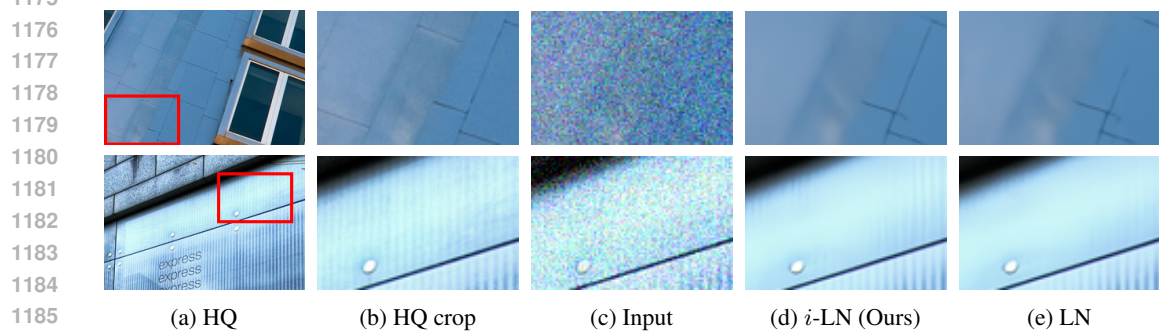
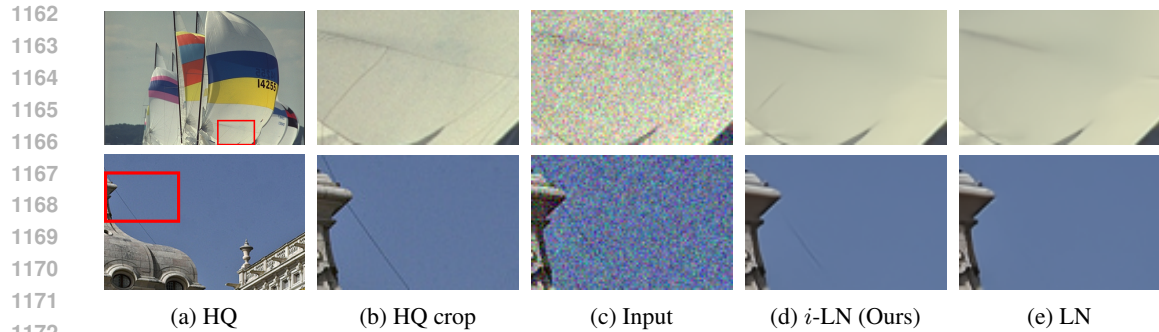
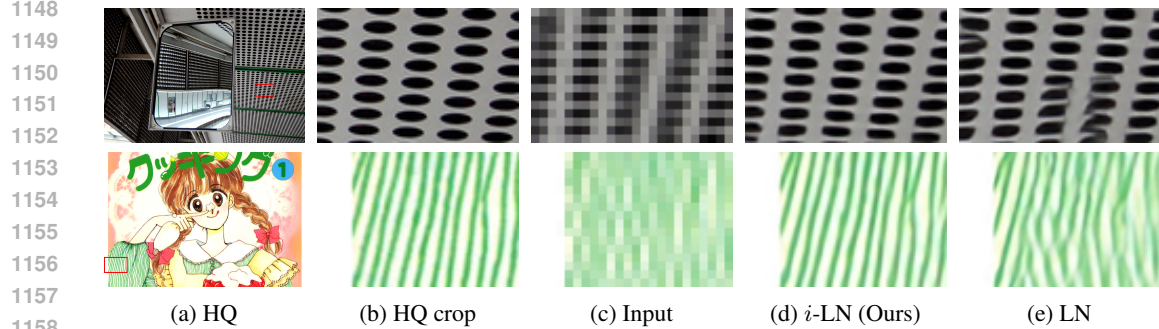
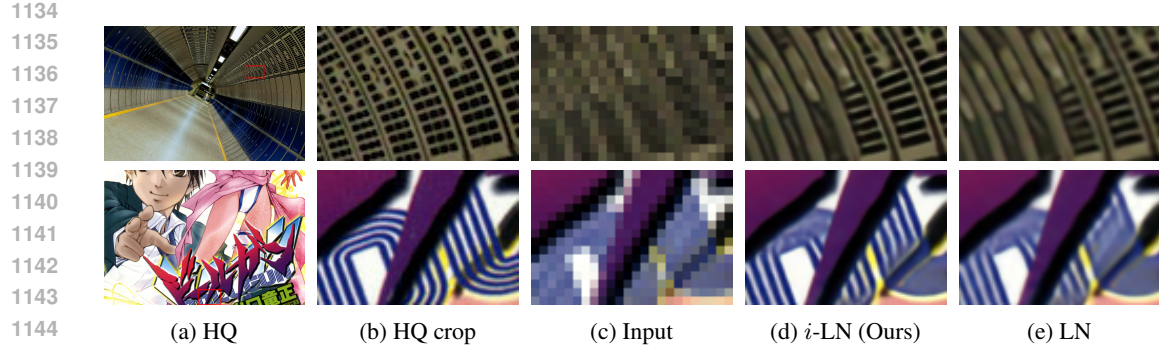
1129

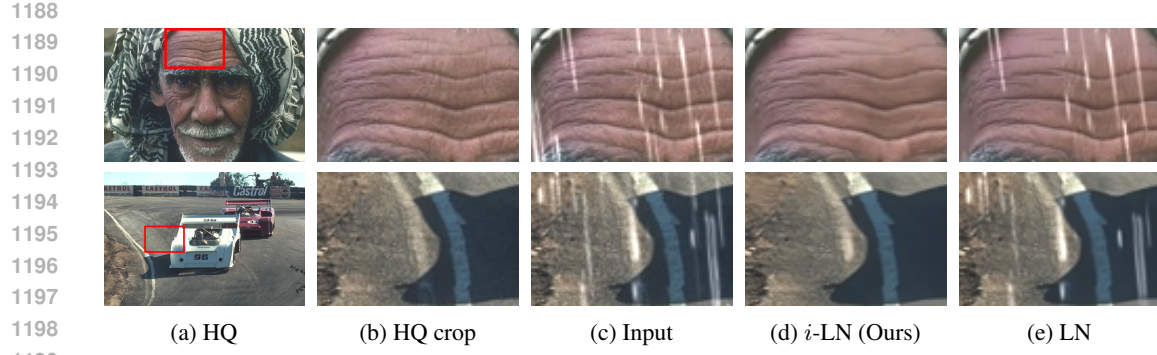
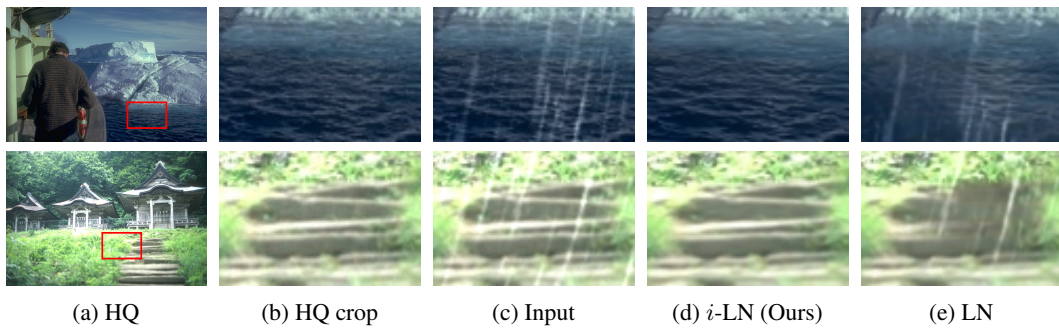
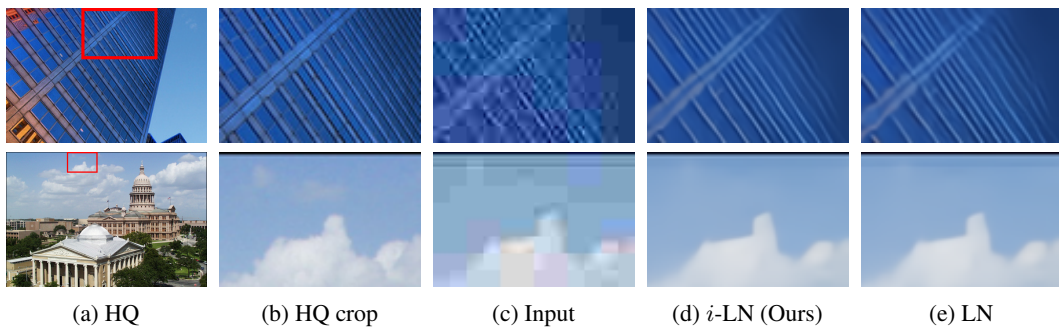
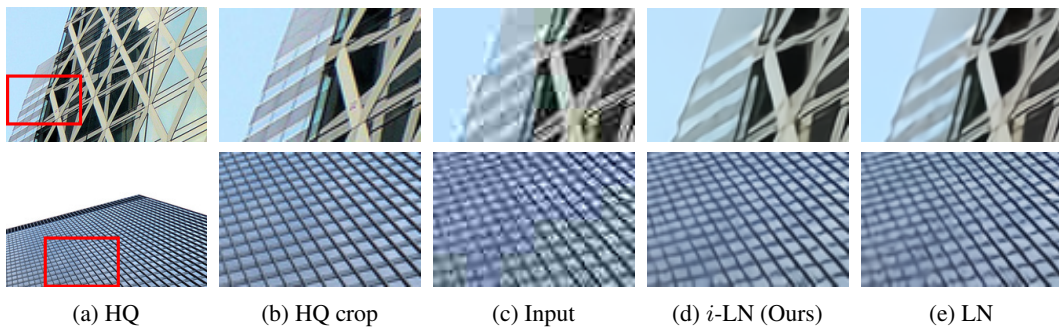
1130

1131

1132

1133



Figure 20: Visual comparison between LN and *i*-LN for the deraining task with HAT₁.Figure 21: Visual comparison between LN and *i*-LN for the deraining task with SwinIR₁.Figure 22: Visual comparison between LN and *i*-LN for the JPEG artifact removal task with HAT₁.Figure 23: Visual comparison between LN and *i*-LN for the JPEG artifact removal task with SwinIR₁.

1242 **G DETAILED DERIVATIONS FOR STRUCTURE PRESERVATION**
1243

1244 **G.1 NOTATION AND PRELIMINARIES**
1245

1246 Let $X \in \mathbb{R}^{L \times C}$ be the feature matrix with tokens $x_\ell \in \mathbb{R}^C$ (row-vectors). Define the inter-pixel
1247 (inter-token) structure by the set of pairwise displacements
1248

$$\Delta X := \{x_\ell - x_k : 1 \leq \ell, k \leq L\}.$$

1249 A map $T : \mathbb{R}^C \rightarrow \mathbb{R}^C$ *preserves inter-pixel structure up to scale* if there exists a homothety
1250 $H(x) = ax + b$ with $a > 0, b \in \mathbb{R}^C$ such that
1251

$$T(x_\ell) - T(x_k) = a(x_\ell - x_k) \quad \text{for all } \ell, k.$$

1252 Equivalently, all angles and pairwise distance ratios are preserved.
1253

1254 We analyze the *pure normalization maps* (i.e., the normalization before the affine (γ, β) is applied);
1255 any global translation by β does not affect ΔX , and a scalar post-scale can be absorbed into the
1256 homothety factor a .
1257

1258 **G.2 PROPOSITION 1 (VANILLA LAYERNORM FAILS TO PRESERVE STRUCTURE)**
1259

1260 Let T_{LN} denote the transformation defined by the normalization in vanilla *per-token* LayerNorm. In
1261 general there do not exist $a > 0$ and an orthogonal Q such that for all tokens x_ℓ, x_k ,
1262

$$T_{LN}(x_\ell) - T_{LN}(x_k) = a Q(x_\ell - x_k).$$

1263 Hence T_{LN} is not conformal on the token set. By the nested class relation Homothety \subset
1264 Similarity \subset Conformal, it follows that T_{LN} is neither a similarity nor a homothety, and thus
1265 does *not* preserve inter-pixel structure in general.
1266

1267 **Proof.** Write per-token means and standard deviations as
1268

$$\mu_\ell = \frac{1}{C} \sum_{c=1}^C x_{\ell,c}, \quad \sigma_\ell = \left(\frac{1}{C} \sum_{c=1}^C (x_{\ell,c} - \mu_\ell)^2 \right)^{1/2}.$$

1269 The pure LN map (no γ, β) acts componentwise as
1270

$$T_{LN}(x_\ell) = \frac{x_\ell - \mu_\ell \mathbf{1}}{\sigma_\ell},$$

1271 so for two tokens ℓ, k ,
1272

$$\Delta_{\ell k} := T_{LN}(x_\ell) - T_{LN}(x_k) \tag{4}$$

$$= \frac{x_\ell}{\sigma_\ell} - \frac{x_k}{\sigma_k} - \left(\frac{\mu_\ell}{\sigma_\ell} - \frac{\mu_k}{\sigma_k} \right) \mathbf{1}. \tag{1}$$

1273 Assume for contradiction there exist $a > 0$ and orthogonal Q such that $\Delta_{\ell k} = a Q(x_\ell - x_k)$ for all
1274 ℓ, k . Compare the coefficients of x_ℓ and x_k on both sides of (1). Because the equality must hold for
1275 arbitrary token values, we must have
1276

$$\frac{1}{\sigma_\ell} I = aQ \quad \text{and} \quad \frac{1}{\sigma_k} I = aQ,$$

1277 hence $\sigma_\ell = \sigma_k$ for all ℓ, k and Q must be proportional to the identity. With $\sigma_\ell \equiv \sigma$, the bias term
1278 in (1) reduces to $(\frac{\mu_k - \mu_\ell}{\sigma}) \mathbf{1}$, which must vanish for all ℓ, k ; thus $\mu_\ell = \mu_k$ for all ℓ, k . Therefore the
1279 assumed similarity can hold only in the *degenerate* case where all tokens share identical per-token
1280 mean and variance.
1281

1282 For real features, $\{\mu_\ell, \sigma_\ell\}$ are not constant across tokens, so the assumption leads to a contradiction.
1283 Hence no single similarity map exists; T_{LN} is not conformal and does not preserve spatial structure.
1284

1285 **Remark.** The degenerate equal-statistics case is precisely the rare exception noted in the main text.
1286

1296 G.3 PROPOSITION 2 (LN* PRESERVES STRUCTURE)
12971298 Let T_{LN^*} denote the transformation defined by the normalization in *spatially holistic* LayerNorm
1299 (LN*) with global mean and standard deviation

1300
1301
$$\mu = \frac{1}{LC} \sum_{\ell,c} x_{\ell,c}, \quad \sigma = \left(\frac{1}{LC} \sum_{\ell,c} (x_{\ell,c} - \mu)^2 \right)^{1/2} > 0.$$

1302

1303 Then for any tokens x_ℓ, x_k ,
1304

1305
$$T_{\text{LN}^*}(x_\ell) - T_{\text{LN}^*}(x_k) = \frac{1}{\sigma}(x_\ell - x_k),$$

1306

1307 so T_{LN^*} is a homothety and preserves inter-pixel structure up to a global scale.
13081309 **Proof.** T_{LN^*} (without γ, β) is
1310

1311
$$T_{\text{LN}^*}(x) = \frac{x - \mu \mathbf{1}}{\sigma}.$$

1312 Hence
1313

1314
$$T_{\text{LN}^*}(x_\ell) - T_{\text{LN}^*}(x_k) = \frac{x_\ell - \mu \mathbf{1}}{\sigma} - \frac{x_k - \mu \mathbf{1}}{\sigma} = \frac{1}{\sigma}(x_\ell - x_k).$$

1315 This is exactly a homothety with scale factor $a = \sigma^{-1}$; therefore angles and pairwise distance ratios
1316 of ΔX are preserved and the spatial configuration is rigid up to a uniform scale.
1317
1318
1319
1320
1321
1322
1323
1324
1325
1326
1327
1328
1329
1330
1331
1332
1333
1334
1335
1336
1337
1338
1339
1340
1341
1342
1343
1344
1345
1346
1347
1348
1349

1350
 1351
 1352
 1353
 1354
 1355
 1356
 1357
 1358
 1359
 1360
 1361
 1362
 1363

Network Architecture Hyperparameters	
Embedding Dimension	60
Layer Depths	[6, 6, 6, 6]
Attention Heads	[6, 6, 6, 6]
Window Size	8×8
MLP Ratio	2
Residual Connection	‘1conv’
Dataset Configuration	
Training Dataset	DIV2K + Flickr2K
PatchSize BatchSize	
- Denoising	$64 \times 64 16$
- Deraining	$128 \times 128 8$
- JPEG Artifact Removal	$64 \times 64 16$
Noise Degradation	<code>torch.randn</code>
JPEG Degradation	OpenCV
Optimizing Configuration	
Total Iterations	300K
Optimizer	Adam
Learning Rate (LR)	2×10^{-4}
Adam Betas	(0.9, 0.99)
Weight Decay	0
Scheduler ($\gamma = 0.5$)	StepLR
Milestones (K)	250
Loss Function	L1 Loss

1378
 1379
 1380
 1381
 1382
 1383
 1384
 1385
 1386
 1387
 1388
 1389
 1390
 1391
 1392
 1393
 1394
 1395
 1396
 1397
 1398
 1399
 1400
 1401
 1402
 1403

Table 10: Hyperparameters and training configurations for the model variant SwinIR₁. Network architectural terminology is based on terminologies either in the official implementation of each work or the implementation in BasicSR Wang et al. (2022b).

Network Architecture Hyperparameters	
Embedding Dimension	96
Layer Depths	[6, 6, 6, 6, 6]
Attention Heads	[6, 6, 6, 6, 6]
Window Size	16×16
MLP Ratio	2
Residual Connection	‘1conv’
Dataset Configuration	
Training Dataset	DIV2K + Flickr2K
PatchSize BatchSize	
- $\times 2$ Super Resolution	$64 \times 64 16$
- $\times 4$ Super Resolution	$128 \times 128 16$
SR Degradation	MATLAB
Optimizing Configuration	
Total Iterations	300K
Optimizer	Adam
Learning Rate (LR)	2×10^{-4}
Adam Betas	(0.9, 0.99)
Weight Decay	0
Scheduler ($\gamma = 0.5$)	StepLR
Milestones (K)	250
Loss Function	L1 Loss

Table 11: Hyperparameters and training configurations for the model variant DRCT₁. Network architectural terminology is based on terminologies either in the official implementation of each work or the implementation in BasicSR Wang et al. (2022b).

1404

1405

1406

1407

1408

1409

1410

1411

1412

1413

1414

1415

1416

1417

1418

1419

Network Architecture Hyperparameters

Embedding Dimension	60
Layer Depths	[6, 6, 6, 6]
Attention Heads	[6, 6, 6, 6]
Window Size	16 × 16
MLP Ratio	2
Compress Ratio	24
Squeeze Factor	24
Overlap Ratio	0.5
Conv Scale	0.01
Residual Connection	‘1conv’

Dataset Configuration

Training Dataset	DIV2K + Flickr2K
PatchSize BatchSize - × 4 Super Resolution	128 × 128 16
SR Degradation	MATLAB

Optimizing Configuration

Total Iterations	300K
Optimizer	Adam
Learning Rate (LR)	2×10^{-4}
Adam Betas	(0.9, 0.99)
Weight Decay	0
Scheduler ($\gamma = 0.5$)	StepLR
Milestones (K)	250
Loss Function	L1 Loss

Table 12: **Hyperparameters and training configurations for the model variant SRFormer₁.** Network architectural terminology is based on terminologies either in the official implementation of each work or the implementation in BasicSR Wang et al. (2022b).

Network Architecture Hyperparameters

Embedding Dimension	96
Layer Depths	[6, 6, 6, 6, 6]
Attention Heads	[6, 6, 6, 6, 6]
Window Size	16 × 16
MLP Ratio	2
Compress Ratio	24
Squeeze Factor	24
Overlap Ratio	0.5
Conv Scale	0.01
Residual Connection	‘1conv’

Dataset Configuration

Training Dataset	DIV2K + Flickr2K
PatchSize BatchSize - Denoising	64 × 64 16
- Deraining	128 × 128 8
- JPEG Artifact Removal	64 × 64 16
- ×2 Super Resolution	64 × 64 16
- ×4 Super Resolution	128 × 128 16
Noise Degradation	torch.randn
JPEG Degradation	OpenCV
SR Degradation	MATLAB

Optimizing Configuration

Total Iterations	300K
Optimizer	Adam
Learning Rate (LR)	2×10^{-4}
Adam Betas	(0.9, 0.99)
Weight Decay	0
Scheduler ($\gamma = 0.5$)	StepLR
Milestones (K)	250
Loss Function	L1 Loss

Table 13: **Hyperparameters and training configurations for the model variant HAT₁.** Network architectural terminology is based on terminologies either in the official implementation of each work or the implementation in BasicSR Wang et al. (2022b).

1458
 1459
 1460
 1461
 1462
 1463
 1464
 1465
 1466
 1467
 1468
 1469

1470
 1471

Network Architecture Hyperparameters	
Embedding Dimension	144
Layer Depths	[6, 6, 6, 6, 6, 6]
Attention Heads	[6, 6, 6, 6, 6, 6]
Window Size	16×16
MLP Ratio	2
Compress Ratio	24
Squeeze Factor	24
Overlap Ratio	0.5
Conv Scale	0.01
Residual Connection	‘1conv’
Dataset Configuration	
Training Dataset	DIV2K + Flickr2K
PatchSize BatchSize - $\times 4$ Super Resolution	$128 \times 128 16$
SR Degradation	MATLAB
Optimizing Configuration	
Total Iterations	500K
Optimizer	Adam
Learning Rate (LR)	2×10^{-4}
Adam Betas	(0.9, 0.99)
Weight Decay	0
Scheduler ($\gamma = 0.5$)	MultiStepLR
Milestones (K)	[250, 400, 450, 475]
Loss Function	L1 Loss

1494
 1495
 1496
 1497
 1498
 1499
 1500
 1501
 1502
 1503
 1504
 1505
 1506
 1507
 1508
 1509
 1510
 1511

Table 14: **Hyperparameters and training configurations for HAT₂.** This variant uses the **HAT-S** architecture but is trained with a reduced budget. Differences from HAT₁ are highlighted in **bold**. Network architectural terminology is based on terminologies either in the official implementation of each work or the implementation in BasicSR Wang et al. (2022b).

Network Architecture Hyperparameters	
Embedding Dimension	180
Layer Depths	[6, 6, 6, 6, 6, 6]
Attention Heads	[6, 6, 6, 6, 6]
Window Size	16×16
MLP Ratio	2
Compress Ratio	3
Squeeze Factor	30
Overlap Ratio	0.5
Conv Scale	0.01
Residual Connection	‘1conv’
Dataset Configuration	
Training Dataset	DIV2K + Flickr2K
PatchSize BatchSize	
- $\times 2$ Super Resolution	$128 \times 128 32$
- $\times 4$ Super Resolution	$256 \times 256 32$
SR Degradation	MATLAB
Optimizing Configuration	
Optimizer	Adam
Adam Betas	(0.9, 0.99)
Weight Decay	0
Scheduler ($\gamma = 0.5$)	MultiStepLR
Loss Function	L1 Loss
$\times 2$ Super Resolution	
- Total Iterations	500K
- Learning Rate (LR)	2×10^{-4}
- Scheduler Milestones (K)	[250, 400, 450, 475]
$\times 4$ Super Resolution	
- Total Iterations	250K
- Learning Rate (LR)	1×10^{-4}
- Scheduler Milestones (K)	[125, 200, 225, 240]
- Pretrained	finetune from $\times 2$ SR weight

Table 15: **Hyperparameters and training configurations for HAT^\dagger** . This variant uses the full-sized HAT architecture and precisely follows the training settings of the public model. Network architectural terminology is based on terminologies either in the official implementation of each work or the implementation in `BasicSR` Wang et al. (2022b).

1512
1513
1514
1515
1516
1517
1518
1519
1520
1521
1522
1523
1524
1525
1526
1527
1528
1529
1530
1531
1532
1533
1534
1535
1536
1537
1538
1539
1540
1541
1542
1543
1544
1545
1546
1547
1548
1549
1550
1551
1552
1553
1554
1555
1556
1557
1558
1559
1560
1561
1562
1563
1564
1565

1566 **H THE USE OF LARGE LANGUAGE MODELS (LLMs)**
15671568 In this study, LLMs were used for text editing, grammar correction, and coding assistance for graph
1569 visualization.
1570

1571

1572

1573

1574

1575

1576

1577

1578

1579

1580

1581

1582

1583

1584

1585

1586

1587

1588

1589

1590

1591

1592

1593

1594

1595

1596

1597

1598

1599

1600

1601

1602

1603

1604

1605

1606

1607

1608

1609

1610

1611

1612

1613

1614

1615

1616

1617

1618

1619